Mechanics of Advanced Composite Structures

Journal homepage: https://macs.semnan.ac.ir/

Semnan University

ISSN: 2423-7043

*Research Article*

# Shift-Robust Machine Learning Surrogate with Importance-Weighted Conformal Prediction for Vibration and Inverse Design of Functionally Graded Porous Tapered Beams

**Satyasaibaba Pitta [a*], Ranga Janardhana Ginka [b], Balakrishna Bhanavathu [c]**

[a,c] *Department of Mechanical Engineering, University College of Engineering, JNTUK, Kakinada-533003, India.*

[b] *Department of Mechanical Engineering, Jawaharlal Nehru Technological University Anantapur, Anantapuramu-515002, India.*



**ARTICLE INFO**

***Article history:***

Received: 2024-10-19
Revised: 2025-03-22
Accepted: 2025-05-12

***Keywords:***

Non-dimensional natural frequency;

Gradient-boosted decision trees;

Risk-aware.

**ABSTRACT**

This study addresses the challenge of designing functionally graded porous tapered beams (FGPTB) whose natural frequencies are highly sensitive to grading, porosity topology, geometry, and boundary conditions. Most existing vibration studies on surrogates optimize only in-distribution accuracy and neglect calibrated reliability under deployment shifts. A machine learning surrogate is needed to deliver accurate, uncertainty-aware predictions of non-dimensional natural frequency (Ω) and to support risk-aware inverse design when boundary conditions, porosity patterns, slenderness, or taper/width ratios differ from the training archive. A higher-order shear deformation theory (HSDT) is used to compute Ω over a Cartesian lattice spanning bi-directional gradient indices (0-10), porosity levels up to 0.3 (even/uneven patterns), aspect ratios 10 and 40, taper and width ratios 0-1.0, and SS/CC supports, yielding 11,616 simulations. Gradient-boosted trees form the backbone regressor, complemented by quantile heads. Split-conformal prediction provides finite-sample valid intervals in-distribution, while importance-weighted conformal recalibrates residual quantiles under covariate shift. Explainability is delivered via uncertainty-aware permutation importance, 1D/2D partial dependence, and isotonic overlays. A bi-objective inverse design screen ranks feasible FGPTB configurations on the Pareto plane of absolute error versus calibrated 90% interval width to select knee solutions under manufacturability constraints. Under 5-fold cross-validation, the surrogate attains MAE=0.56, RMSE=0.91, and $R^2$=0.9996. Split-conformal intervals under cover in cross-boundary and regime holdout tests, whereas importance-weighted conformal restores coverage to 0.90 with modest width inflation. Boundary conditions and grading dominate Ω, porosity monotonically lowers Ω, and taper/width increases Ω with diminishing returns. Low-frequency targets are met with tight intervals, mid-frequency targets require relaxing porosity/geometry or supports, and high-frequency targets trigger calibrated interval inflation, signalling capacity limits. The workflow converts calibrated uncertainty into actionable vibration design decisions for FGPTB and can be extended to higher modes and coupled responses.



## 1. Introduction

Functionally graded porous beams (FGPB) are increasingly deployed where lightweight must coexist with tight vibration limits, yet their vibration dynamics remain highly sensitive to coupled variations in gradation, porosity distribution, and non-uniform cross-sections under practical boundary conditions [1]. Recent studies have advanced formulations for this class of members, such as the modal analyses of functionally graded porous/non-porous beams

based on Timoshenko/Euler-Bernoulli kinematics and Hamilton's principle, together with systematic parametric sweeps over porosity patterns and taper ratios [2]. These studies clarify trend directions (frequency reductions with porosity, nontrivial interactions with taper/width) and provide validated reference solutions across Simply Supported (SS), Clamped-Clamped (CC), and Pinned regimes [3]. Parallel developments report third-order shear and related higher-order theories tailored to bi-directional FGPB, highlighting the need to capture shear effects, thickness-wise gradation, and boundary condition sensitivity in any predictive workflow [4]. At the same time, composite-structure design increasingly adapts Machine Learning (ML) surrogates to accelerate dynamics and optimization, but most recent efforts emphasize in-distribution accuracy rather than calibrated reliability when the target regime (e.g., porosity pattern, aspect-ratio bin, or boundary condition) shifts from the training archive.

Functionally graded materials (FGM) employ continuous spatial gradation of constituents to tailor stiffness and mass distributions and mitigate stress concentrations. In porous functionally graded beams, controlled void patterns further reduce density while modifying elastic moduli, producing frequency responses that depend on gradation indices, porosity pattern/level, and section geometry [5]. Variable cross-section FGPBs display mode-frequency shifts governed by the competing effects of bending rigidity and lineal inertia, with taper/width changes altering both fields along the span [6]. Analytical and Ritz-type formulations for bi-directional FGP beams report systematic frequency reductions with increasing porosity (across even/uneven patterns) and sensitivity to gradation in two directions, under canonical supports, while confirming that the choice of beam theory (CBT/FSDT/HSDT) influences quantitative predictions [7]. For beams with variable cross-section, an increase in local thickening or width tends to increase the natural frequency, whereas thinning or aggressive taper can reduce it. These trends persist under SS and CC conditions, commonly used in benchmarks [8]. Extensions to microscale and tri-directionally graded beams reinforce the same dependencies and Boundary Condition (BC) sensitivity in refined kinematics [9].

In parallel, HSDTs and intelligent algorithms (IA) have been integrated to systematize model selection in plate and beam analysis. Mantari et al. proposed a neural network and multi-objective genetic algorithm methodologies to construct "best theory diagrams", enabling the automatic selection of the most appropriate shear deformation theory as a function of geometric and loading parameters [10]. Subsequent contributions introduced generalized two unknown HSDT formulations for isotropic and orthotropic plates [11], a four unknown arctangent exponential shear deformation theory tailored to functionally graded plates [12], and quasi-3D hybrid five and six unknown HSDTs for advanced composite and sandwich plates [13-15]. These studies emphasize that both the kinematic richness (2/4/5/6 unknowns) and the intelligent selection of the underlying theory are critical modelling decisions in refined shear deformation methodologies. For tapered members, Canales and Mantari [16] carried out elasto-plastic vibrational analysis of tapered bars under uniform axial loading while accounting for shear deformation and rotary inertia, highlighting that taper, shear effects, and material nonlinearity jointly govern frequency evolution.

Functionally graded (FG) and porous beams and plates have been analyzed extensively using refined beam and plate theories. Early and recent works by Vo et al. developed refined shear deformation models and finite element formulations for static, buckling, and vibration of FG and FG sandwich beams, highlighting the strong influence of shear effects, boundary conditions, and gradient indices on the frequency spectrum [17,18]. Mesbah et al. [19] and Wang and Li [20] studied free vibration of FGM beams using Levinson and higher-order shear deformation beam theories, demonstrating the need for enriched kinematics to capture thickness stretching and higher-order shear contributions. For porous systems, Chen et al. [21] analyzed free and forced vibrations and buckling of shear deformable FGPBs, while subsequent reviews and extensions by Chen et al. [22] and Wu et al. [23] systematically surveyed mechanical analyses, design routes, and applications of FGP structures. More recent

studies have examined thermal vibration, size-dependent dynamics, and non-local effects in FGP beams and nanobeams, further broadening the modelling landscape [24-26]. These works establish a mature baseline for deterministic vibration analysis of FG and FGP structures, but typically focus on high-accuracy mechanics rather than data-driven surrogates or calibrated uncertainty under deployment shifts.

Beyond purely elastic responses, viscoelasticity and randomness have been incorporated into FGM vibration models. Three-dimensional elastic and viscoelastic formulations have been proposed for layer-wise in-plane FG orthotropic plates, revealing strong coupling between grading, damping, and mode shapes [27]. Time-domain solution methods based on Bernstein polynomials and fractional operators have been developed for viscoelastic FGBs under various boundary conditions [28], and viscoelastic nanobeam models have been formulated to quantify scale-dependent damping effects [29]. In parallel, forced vibration of FGP beams on viscoelastic foundations has been investigated, illustrating porosity and foundation parameters that interact with rheological behaviour [30]. Stochastic methods such as the stochastic nonlinear free vibration of FGBs with uncertain material properties and thermal loading, as well as stochastic vibration and buckling of FG and FGP sandwich beams or nanobeams with random grading, porosity, and geometric parameters, have been reported [31,32]. These viscoelastic and stochastic studies address material damping and parametric uncertainty but generally rely on intrusive stochastic FEM or semi-analytical schemes rather than non-intrusive ML surrogates with finite sample coverage guarantees.

Machine learning surrogates have recently been introduced to accelerate vibration analysis of FG and FGP structures. Wu et al. combined a mixed finite element formulation with a comparative artificial neural network to approximate the nonlinear free vibration response of FGBs [33]. Semi-analytical models for size-dependent dynamics and free vibration of porous or bi-directional FG nanobeams have been coupled with ML regressors to map high-dimensional design spaces to natural frequencies under various boundary conditions [34,35]. For FGP nanobeams, thermal vibration analyses using boosting-based ML models and semi-analytical solvers have demonstrated that ensemble methods (e.g., gradient boosting and related tree-based ensembles) can yield accurate predictions across a wide range of temperature, porosity, and gradient indices [36]. More broadly, recent work on ML for FGPB has benchmarked different ML paradigms, including boosting, against traditional surrogate models for structural responses [37]. These studies confirm the value of ML in FGM vibration, but typically prioritize pointwise accuracy, assume in-distribution deployment, and provide limited treatment of calibrated uncertainty or risk-aware inverse design.

In parallel, physics-informed neural networks (PINNs) and other scientific ML approaches have been extensively explored for structural dynamics. PINN formulations have been proposed to simulate transverse vibrations of beams and to identify dynamic parameters directly from governing equations and sparse measurements [38]. Physics-informed deep networks have also been applied to bending and free vibration of functionally graded or 2D-FG nano-beams, combining nonlocal or strain gradient elasticity with Hamilton's principle in the loss functional [39,40]. Other PINN-based studies address forced vibrations of beams with variable cross sections, viscoelastic or composite plates, and coupled bending and vibration problems [40,41]. Recent reviews on scientific ML for FGPBs position PINNs, deep operator networks, and related architecture as promising tools for directly solving constrained vibration problems using partial differential equations [42].

Current vibration studies on FGPBs and tapered members provide accurate deterministic predictions using refined shear deformation theories, viscoelastic and stochastic formulations, and, more recently, ML and PINN-based surrogates, but almost all are tuned for in-distribution accuracy and nominal operating regimes. Existing ML surrogates for FG/FGP vibration typically neglect finite sample and valid uncertainty quantification, to explicitly handle covariate shifts in boundary conditions, porosity topology, slenderness or geometry, and rarely connect predictive models to risk-aware inverse design. For functionally graded porous tapered beams (FGPTB) in particular, there remains no

compact, tabular surrogate that couples advanced boosting methods with conformal calibration to maintain coverage under deployment shifts while supporting explainable, uncertainty-aware vibration design.

The novelty of the present study lies in developing a shift-robust ML surrogate for vibration analyses of FGPTB that integrates gradient-boosted trees with split and importance-weighted conformal calibration and embeds physics-aligned explainability (permutation importance and 1D/2D partial dependence with isotonic overlays) to provide calibrated, interpretable predictions under covariate shift and to enable risk-aware inverse design.

The objectives of this study are as follows:

1. Develop a shift-robust ML surrogate for the non-dimensional natural frequency (Ω) of Functionally Graded Porous Taper Beam (FGPTB) by integrating gradient-boosted trees with split- and importance-weighted conformal calibration to preserve nominal coverage under covariate shift.
2. Establish rigorous generalization tests, including cross-boundary condition transfers and regime holdouts in porosity pattern, slenderness, and geometry extremes, to demonstrate reliability beyond IID settings.
3. Embed physics-aligned explainability through permutation importance and 1D/2D partial dependence analyses with isotonic overlays to verify and enforce expected vibration trends.
4. Demonstrate a risk-aware inverse design workflow that selects manufacturable configurations on the Pareto frontier of absolute error versus calibrated 90 % interval width, enabling uncertainty-aware vibration design decisions.

The study spans a broad parametric lattice of bi-directional gradient indices. $P_x, P_z$ from 0-10, porosity levels up to 0.3 in both even and uneven patterns, aspect ratios (AR) of 10 and 40, taper and width ratios from 0 to 1.0, and both SS and CC BCs capturing the dominant geometric and material drivers of FGPTB vibration.

The remainder of this paper is organized as follows. Section 2 presents the higher-order shear deformation formulation of the FGPTB and the associated free vibration eigenproblem. Section 3 describes the construction of the parametric design lattice, the supervised dataset, and the learning task definition. Section 4 details the ML methodology, including the gradient-boosted tree surrogate, split and importance-weighted conformal calibration, generalization protocols, explainability, and risk-aware inverse design procedures. Section 5 reports predictive accuracy, cross-boundary and regime holdout performance, calibration behaviour, and inverse design results. Section 6 discusses target domain coverage restoration, physics alignment, and empirical vibration trends, while Section 7 outlines the main limitations of the present study. Section 8 concludes the work and sketches directions for extending the methodology to richer physics and broader design spaces.

## 2. Theory and Formulation of Functionally Graded Porous Taper Beam

### *2.1. Geometry and Kinematics of Functionally Graded Porous Taper Beam*

An FGPTB of length $L$ with linearly varying thickness and width along the span is considered in this study. Let $X$ denote the beam axis, $Z$ the thickness coordinate, and $Y$ the width direction. The taper ratio prescribes a linear law for the thickness variation from $h_1$ at one end to $h_2$ at the other $(h_1 > h_2)$ analogously, the width ratio governs a linear law from $b_1$ to $b_2$. The taper ratio and width ratio compactly encode the geometric non-uniformity used later in the dataset as 'tap' and 'wid', respectively. The material gradation is two-directional with a pair of gradient indices $(P_x, P_z)$ that controls constituent distribution along $X$ and through the thickness $Z$, respectively, so that effective properties vary coherently with the geometry.

The modeling assumptions are such that the material properties, Young's modulus $(E)$, mass density $(\rho)$, and Poisson's ratio $(\nu)$ vary continuously according to power-law gradation across the thickness and width directions. No mass transfer occurs at phase interfaces, which ensures a smooth stiffness inertia field and is consistent with standard mixture rules for FGMs with porosity. Higher-order shear deformation theory (HSDT) in which higher-order terms are retained in the displacement field, and transverse shear is not assumed constant through the

thickness. Instead, a shear shape function is introduced so that the transverse shear stress satisfies the required thickness surface conditions. The in-plane and transverse displacements are represented by polynomial functions in the thickness coordinate, enabling accurate through-thickness kinematics without arbitrary shear correction factors. The FGPTB model is shown in Fig. 1.

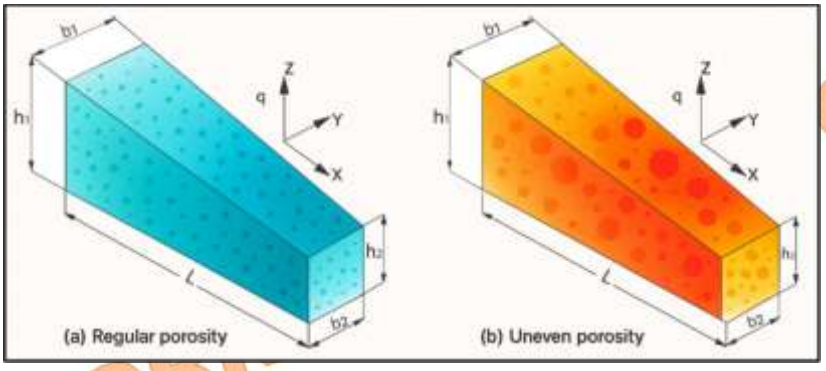


**Fig. 1.** Two-directional functionally graded taper porous beam model

The axial, $u(x,z)$ and transverse displacements, $w(x,z)$ at a generic point are constructed from the mid-surface variables (axial displacement and rotation) supported by the HSDT thickness functions. The shear shape function governs the distribution of shear deformation across the thickness. The corresponding strain-displacement relations follow the HSDT form, as shown in Eqs. (1) and (2), and provide the basis for stress recovery and energy functionals [43].

$$u(x,z) = u_0(x) + z\emptyset(x) - f(z;h)\left(\emptyset(x) + w_{0,x}(x)\right) \quad (1)$$

$$w(x,z) = w_0(x) \quad (2)$$

here $u(x,z)$ and $w(x,z)$ are the axial and transverse displacements at the given point $(x,z)$, respectively. $u_0(x)$ is the axial displacement at the neutral axis of the beam, $\emptyset(x)$ is the rotation of the cross-section due to bending and $f(z)$ [44] is the shear shape function, as per Reddy's HSDT, which characterizes the shear deformation distribution across the thickness of the FGPTB, satisfying the necessary boundary conditions.

$$f(z;h) = \frac{4z^3}{3h^2} \quad (3)$$

$$g(z;h) = 1 - f'(z) = 1 - \frac{4z^2}{h^2},$$

$$g\left(\pm {}^{h}/_{2};h\right) = 0$$

$g(z;h)$ is the shear shape derivative.

Nonlinear strain-displacement relations, Eqs. (4) and (5) are adopted to accommodate moderate geometric nonlinearity in kinematics, while the constitutive law is taken as linear elastic (Hooke's law) with functionally graded effective properties as shown in Eqs. (6) and (7) [45].

$$\varepsilon_x = u_{0,x} + z\emptyset_{,x} - f(z;h)(\emptyset_{,x} + w_{0,xx}) \quad (4)$$

$$\gamma_{xz} = g(z;h)(\phi + w_{0,x}) \quad (5)$$

$$\sigma_x = E(x,z)\varepsilon_x \quad (6)$$

$$\tau_{xz} = G(x,z)\gamma_{xz}, \qquad G = \frac{E}{2(1+\nu)} \quad (7)$$

### *2.2. Material Gradation and Porosity*

The effective properties of the FGPTB are obtained from a power-law mixture of metal $(m)$ and ceramic $(c)$ phases with two-directional gradation. Let $V_m$ and $V_c$ denote the local volume fractions of metal and ceramic, respectively. The volume fraction constraint is shown in Eqs. (8) and (9).

$$V_m(x,z) + V_c(x,z) = 1 \quad (8)$$

$$V_m(x,z) = \left(\frac{x}{L}\right)^{P_x}\left(\frac{1}{2} + \frac{z}{h(x)}\right)^{P_z}, V_c = 1 - V_m \quad (9)$$

The effective Young's modulus $E(x,z)$, Poisson's ratio $\nu(x,z)$ and mass density $\rho(x,z)$ of the FGPTB under even and uneven porosity distributions is calculated using Eqs. (10) to (12) [45].

$$E(x,z) = (E_c - E_m)V_c(x,z) + E_m - \frac{\alpha}{2}(E_c + E_m)s(z) \quad (10)$$

$$\nu(x,z) = (\nu_c - \nu_m)V_c(x,z) + \nu_m - \frac{\alpha}{2}(\nu_c + \nu_m)s(z) \quad (11)$$

$$\rho(x,z) = (\rho_c - \rho_m)V_c(x,z) + \rho_m - \frac{\alpha}{2}(\rho_c + \rho_m)s(z) \quad (12)$$

where, $s(z) = \begin{cases} 1 \\ 1 - \frac{2|z|}{h(x)}, \end{cases}$ for even and uneven patterns, respectively, and $\alpha$ is the porosity index ($0<\alpha<0.3$), which modulates the effective properties to reflect controlled voids in the FGM matrix.

### *2.3. Free Vibration Formulation*

The free vibration of the FGPTB is posed via Hamilton's principle over the time interval. $[t_1, t_2]$ as shown in Eq. (13) [46].

$$\delta \int_{t_1}^{t_2} (T - U)dt = 0 \quad (13)$$

where $T$ and $U$ are the kinetic and strain energies, respectively. External work is absent for the free case. With functionally graded porous properties $E(x,z)$, and $\nu(x,z)$, the strain and kinetic energies are shown in Eqs. (14) and (15).

$$U = \frac{1}{2}\int_{\Omega} [\varepsilon_x E \varepsilon_x + \gamma_{xz} G \gamma_{xz}]\, dzdx \quad (14)$$

$$T = \frac{1}{2}\int_{\Omega} \rho\, \dot{u}^T \dot{u} dzdx \quad (15)$$

Weak form and semi-discretization introduce a vector of generalized degrees of freedoms $q(t)$ through a Ritz expansion that satisfies the BCs (SS or CC) and the beam kinematics as shown in Eq. (16).

$$u(x,z,t) \approx N(x,z)q(t) \quad (16)$$

where $N$ collects spatial trial functions.

Substitution into $U$ and $T$, followed by Hamilton's principle and standard integration over the graded, tapered cross-section, yields the matrix form as shown in Eq. (17).

$$M\ddot{q} + Kq = 0 \quad (17)$$

with $M = \int_{\Omega} \rho\, N^T N dzdx$ and $K = \int_{\Omega} (B^T E(x,z) B + B_s^T G(x,z) B_s)\, dzdx$

here $B$ and $B_s$ are the strain-displacement operators mapping $q$ to $\sigma$ and $\tau$. Through $E(x,z)$, and $\rho(x,z)$ and the geometry $b(x)$, $h(x)$ both $M$ and $K$ depend on the bi-directional gradation $(P_x, P_z)$, porosity (level/pattern), and the taper/width ratios.

Harmonic motion, $q(t) = \phi e^{i\omega t}$ gives the generalized eigenproblem as shown in Eq. (18).

$$(K - \omega^2 M)\phi = 0 \quad (18)$$

$$\phi_n^T M \phi_m = 1, \phi_n^T K \phi_m = \omega_n^2 \delta_{nm}$$

The non-dimensional natural frequency $\Omega$ is estimated using Eq. (19).

$$\Omega = \omega_n \sqrt{m^*/_{k^*}} \quad (19)$$

$$m^* = \int_0^L \int_{A(x)} \rho(x,z) dA dx$$

and

$$k^* = \int_0^L \int_{A(x)} E(x,z) dA \frac{dx}{L}$$

BCs (SS/CC) are applied via the admissible trial space $N$ for essential constraints and via natural boundary terms in the weak form.

### *2.4. Design Space Used to Generate the Dataset*

To sample the regimes that strongly control vibration in FGPTB, the study adopts a Cartesian product of discrete grids over the principal inputs, i.e., the bi-directional grading indices ($P_x, P_z$=1, 5, 10), aspect ratio (AR=10, 40), porosity level ($\alpha = 0, 0.1, 0.2, 0.3$), with through-thickness pattern (even and uneven), taper ratio, and width ratio (0, 0.1, 0.2, 0.3, 0.4, 0.5, 0.6, 0.7, 0.8, 0.9, 1.0), and BCs (SS and CC). For each grid point, the $\Omega$ is evaluated using the HSDT formulation. The resulting table inputs and $\Omega$ for every admissible combination serves as the supervised dataset (11,616 data points) for the ML analysis, as shown in Table S1 in the Supplementary file. The factor set reflects the dominant physical levers reported in recent FGM/FGP beam literature [47].

## 3. Dataset and Problem Definition

### *3.1. Response Definition and Predictors*

For each configuration, the generalized eigenproblem is estimated using Eq. (18). The supervised response is the $\Omega$. Each datum records

the design, grading, porosity, geometry, and support descriptors as shown in Eq. (20).

$$F = (P_x, P_z, AR, \alpha, Por_{pat}, tap, wid, BC) \quad (20)$$

Preprocessing was performed so that all inputs to the surrogate are constructed from the raw design variables (bi-directional gradient indices $P_x, P_z$, porosity level, aspect ratio, taper ratio, and width ratio, boundary condition, and porosity pattern) together with the physics-guided composite features. Categorical factors (boundary condition: SS/CC; porosity pattern: even/uneven) are encoded as one-hot indicator variables. Continuous predictors (raw and composite) are standardized within each outer split using feature-wise affine transforms $z_f = (f - \mu_f)/\sigma_f$, where $\mu_f$ and $\sigma_f$ are the mean and standard deviation computed from the training partition only and then applied unchanged to validation, calibration, and test data. This prevents information leakage across splits. The dataset contains no missing values, so no imputation is required. The entire preprocessing pipeline (feature construction, one-hot encoding, and standardization) is re-fitted inside each cross-validation or transfer scenario using training only statistics.

In addition to these variables, the learning model ingests low-complexity, physics-guided summaries that capture coupled stiffness-inertia trends such as $GI_{sum} = P_x + P_z$, $GI_{prod} = P_x \times P_z$ and $(AR)^{-1}$ along with a restricted set of interactions (e.g., $\alpha \times tap$, $\alpha \times wid$, $tap \times wid$) and squared terms (e.g., $P_x^2, P_z^2$).
where $P_x$ and $P_z$ are the in-plane and through-thickness gradient indices.

For the bi-directional power law used here, increasing $P_x$ or $P_z$ shifts material from metal to ceramic, raising the effective Young's modulus and bending rigidity while only mildly increasing mass density. $GI_{sum}$ therefore, acts as a coarse proxy for overall ceramic richness (net stiffness amplification), whereas $GI_{prod}$ emphasises cases in which both directions are strongly graded, and the section is stiffened simultaneously in span and thickness. Because the fundamental frequency of tapered beam scales over the span, and these composites provide low-dimensional, monotone surrogates for the combined stiffness and inertia effect of bi-directional grading. Including $GI_{sum}$ and $GI_{prod}$ as explicit predictors make the boosted surrogate more sample efficient and yield partial dependence shapes that align with expected FGPTB vibration physics (increasing $\Omega$ for larger $GI_{sum}$ and $GI_{prod}$). Similarly, simple products such as $tap \times wid$ summarise how taper and width jointly redistribute cross-sectional areas and second moments of area along the span, which directly control both bending rigidity and lineal inertia in the FGPTB and therefore its natural frequencies [48]. Categorical factors are encoded as indicator variables (e.g., BC=SS/CC, $Por_{pat}$=even/uneven). Continuous predictors are standardized by feature-wise affine transforms $a \mapsto (a - \mu_a)/\sigma_a$ using training-fold statistics, preventing leakage. where, $a$ is the single raw value of a given feature, $\mu_a$ is the mean of that feature, computed on the training data only, $\sigma_a$ is the standard deviation of that feature, computed on the same training subset. Categorical variables are one-hot encoded. Each continuous feature $x$ is standardized within fold as,

$$\bar{x} = \frac{x - \mu_{train}(x)}{\sigma_{train}(x)}$$

with $\mu_{train}$ and $\sigma_{train}$ computed only on the training partition of each fold/transfer and then applied to test, validation, and target-domain data.

### *3.2. Learning Task*

Let $f: X \longrightarrow R$ be a surrogate mapping feature to $\Omega$ and, when calibrated uncertainty is reported, let $(L, U): X \longrightarrow R^2$ denote a prediction interval at a nominal level. The learning objectives are shown in Eqs. (21) and (22).

$$Accuracy: minE\left|\hat{\Omega} - \Omega\right| \quad (21)$$

$$Calibration: P\{\Omega \in [L, U]\} \approx nominal \quad (22)$$

with sharpness promoted by minimizing the expected interval width $E[U - L]$ for a fixed nominal level.

### *3.3. Data Splits and Evaluation Protocols*

Three complementary protocols are used to quantify both in-distribution performance and robustness to distribution shift.

#### *3.3.1 Random Cross-validation*

A k-fold cross-validation (CV) (stratified on BC and $Por_{pat}$) estimates average generalization error under IID assumptions. All preprocessing

(encoding, scaling, feature construction) is performed within-fold, never on calibration/test.

#### 3.3.2 Cross-boundary Conditions Generalization

Two asymmetric transfers are formed, SS to CC (train on SS, test on CC) and CC to SS (train on CC, test on SS). This isolates the BC shift, known to alter curvature and shear distributions, and therefore modal trends. The calibration pool is drawn from the training BC, and importance-weighing adapts to the target BC. Performance under these transfers gauges robustness to a practically important, label-preserving domain shift.

#### 3.3.3 Regime Holdouts

Three stress tests are defined to probe extrapolation Porosity-pattern-out where train on one pattern (even or uneven) and test on the other. AR-bin-out where train on a subset of aspect-ratio bins, test on held-out bins (slenderness shift), i.e., train on AR=10, test on AR=40 and vice-versa. Extremes in tap/wid are trained on central quantiles, tested on extreme quantiles to assess non-prismatic limits, i.e., train on the central quantiles $tap, wid \in [0.1,0.9]$ and test on extremes $[0,0.1) \cup (0.9,1.0]$. For each protocol, Mean Absolute Error (MAE), Root Mean Squared Error (RMSE), and coefficient of determination ($R^2$), empirical coverage at 1-$\alpha$=0.9, and the mean interval width is estimated.

### 3.4. Evaluation Metrics

The following error metrics are used to evaluate the surrogate performance MAE, Eq. (23), RMSE, Eq. (24), and $R^2$, Eq. (25).

$$MAE = \frac{1}{n}\sum_{i=1}^{n}\left|\hat{\Omega} - \Omega\right| \tag{23}$$

$$RMSE = \sqrt{\frac{1}{n}\sum_{i=1}^{n}\left(\hat{\Omega} - \Omega\right)^2} \tag{24}$$

$$R^2 = 1 - \frac{\sum_i\left(\hat{\Omega} - \Omega\right)^2}{\sum_i\left(\hat{\Omega} - \bar{\Omega}\right)^2} \tag{25}$$

here, $n$ is the number of test samples, $\hat{\Omega}$ is the model-predicted non-dimensional natural frequency, $\bar{\Omega}$ is the mean of the true non-dimensional natural frequencies. Uncertainty is assessed via reliability (empirical coverage vs. nominal) and sharpness (mean interval width), reported overall and by relevant slices (BC, porosity pattern, AR bins). Finally, all metrics are computed under IID splits and shifted regimes (cross-BC, holdouts) to evidence robustness beyond in-distribution fitting.

## 4. Machine Learning Methods

### 4.1. Gradient Boosting Regressor Model

The surrogate adopts Gradient-boosted decision trees (GBDT) as the backbone for tabular regression. Let $f(x) = \sum_{t=1}^{T}\eta h_t(x)$, where $h_t$ are shallow classification and regression trees and $\eta \in (0,1]$ is the learning rate. Trees are added stage-wise to minimize a chosen loss via functional gradient descent; shrinkage, column/row subsampling, and early stopping control variance. Contemporary benchmarks continue to demonstrate GBDT families [49]. The mean regressor is a GBDT trained with a symmetric loss (squared error or Huber). In practice, the Huber loss can improve robustness to heavy-tail residuals without sacrificing bias. Hyperparameters (number of trees, depth/leaves, learning rate, subsampling) are tuned by inner CV with early stopping on a validation fold. Recent studies likewise rely on boosted trees as primary point estimators for physical response variables [50]. The squared error form is shown in Eq. (26).

$$min_f \frac{1}{n}\sum_{i=1}^{n}(y_i - f(x_i))^2 \tag{26}$$

GBDT updates along with residuals $r_i^{(t)}$ are shown in Eq. (27).

$$r_i^{(t)} = y_i - f^{(t-1)}(x_i) \tag{27}$$

To quantify uncertainty without resorting to Bayesian ensembles, two quantile GBDT heads are trained separately at $\beta = 0.05$ and $\beta = 0.95$ using the pinball (quantile) loss, yielding a nominal 90% prediction interval $[\hat{q}_{0.05}(x), \hat{q}_{0.95}(x)]$ as shown in Eq. (28).

$$min_{q_\beta}\frac{1}{n}\sum_{i=1}^{n}\rho_\beta\left(y_i - q_\beta(x_i)\right), \rho_\beta = u(\beta - 1\{u < 0\}) \tag{28}$$

Recent work formalizes and extends quantile boosting (including composite/multi-quantile training and smooth surrogates for the non-differentiable pinball loss), demonstrating practical, high-quality quantile estimation with XGBoost-style learners [51]. XGBoost-style GBDT for the mean and two separate quantile heads at $T \in \{0.05,0.95\}$, yield a nominal 1−α=0.90 interval $[\hat{q}_{0.05}(x), \hat{q}_{0.95}(x)]$. Early stopping (rounds=200 patience) on a fold-internal validation split prevents leakage. Hyperparameters are selected by inner CV over $trees \in [200,1200]$, max $\_depth \in \{4,6,8\}$, learning_rate ∈ {0.03,0.06,0.1}, sub_sample ∈ {0.6,1.0}, colsample_bytree ∈ {40.5,1.0}.

The model training and calibration protocol is executed such that the backbone surrogate is a gradient-boosted decision tree regressor (GBDT) for the conditional mean of Ω, trained with a symmetric loss (squared error or Huber) and regularization through learning rate, tree depth, and subsampling parameters. Two additional GBDT models are trained to estimate the lower and upper quantiles of Ω using the pinball loss, yielding nominal 90 % prediction intervals. Hyperparameters (number of trees, maximum depth, learning rate, row/column subsampling, and minimum child weight) are selected via a small grid search combined with inner cross-validation on the training data, with early stopping based on validation loss to avoid overfitting. For each outer evaluation scenario (5-fold cross-validation and the various transfer tests), the data are first partitioned into a train subset and a calibration subset. The mean and quantile GBDTs are fitted on the train subset only. Split-conformal or importance-weighted conformal prediction is then applied to residuals on the calibration subset to obtain finite-sample valid prediction intervals in the corresponding target regime. Random seeds are fixed, and the splits are stratified by boundary condition and porosity pattern to ensure reproducible training and calibration across all runs.

### *4.2. Calibration of the Model*

The calibration of the model equips the point predictor with finite-sample valid prediction intervals and then adapts them to covariate shift (e.g., SS to CC and CC to SS transfers). Two complementary tools are used split-conformal prediction on residuals and an Importance-weighted (IW) conformal variant based on a lightweight density-ratio classifier. Both are model-agnostic and integrate with the gradient-boosting regressors.

#### *4.2.1 Split-conformal Intervals (Residual Quantiles)*

The dataset is split into train and calibration sets. The mean regressor $\hat{\mu}(x)$ is trained on the train set only. On the calibration set $\{(x_i, y_i)\}_{i=1}^{\eta_{cal}}$ compute nonconformity scores $s_i$ as shown in Eq. (29).

$$s_i = |y_i - \hat{\mu}(x_i)| \tag{29}$$

Let $k = \lceil(\eta_{cal} + 1)(1-\beta)\rceil$ and let $q_{1-\beta}$ be the kth order statistic of $\{s_i\}$. For a new $x_*$, the two-sided split-conformal interval is $\left[\hat{\mu}(x_*) - q_{1-\beta}, \hat{\mu}(x_*) + q_{1-\beta}\right]$ which attains distribution-free (1-$\beta$) marginal coverage under exchangeability, i.e., IID between calibration and target points. When residuals are markedly asymmetric, asymmetric residuals may be used as shown in Eq. (30).

$$s_i^- = \hat{\mu}(x_i) - y_i, s_i^+ = y_i - \hat{\mu}(x_i) \tag{30}$$

This takes the quantiles $q_{1-\beta l}(\{s_i^-\})$, $q_{1-\beta u}(\{s_i^+\})$ with $\beta l + \beta u = \beta$ to form $\left[\hat{\mu}(x_*) - q_{1-\beta l}, \hat{\mu}(x_*) + q_{1-\beta u}\right]$. Recent studies have deployed split-conformal as the default calibration layer (including in survival and network-assisted regression settings), emphasizing its black-box nature and finite-sample validity [52]. When the quantile heads are used, Conformalized Quantile Regression (CQR) is adapted optionally to split-conformally the quantile residuals to correct finite-sample miscalibration while preserving heteroscedastic shapes.

#### *4.2.2 Importance-weighted Conformal Under Covariate Shift*

When the calibration covariates and the target covariates differ, for example, training on SS and testing on CC, the split-conformal interval may mis-cover. A logistic domain classifier $s(x) = Pr(target|x)$ on calibration vs. target covariates with balanced class priors (0.5/0.5). The stabilized importance weight is presented in Eq. (31) clipped to $w_{min}, w_{max}$ followed by self-normalization $\tilde{w}_i = w_i / \sum_j w_j$.

$$w(x) = \frac{s(x)}{1-s(x)}, (w_{min} = 0.1, w_{max} = 10) \quad (31)$$

The Effective Sample Size, $ESS = (\sum \widetilde{w}_i)^2 / \sum \widetilde{w}_i{}^2$ and cap clipping tighter if $ESS < 0.3n_{cal}$. Weighted empirical quantiles of calibration residuals are then set as the Importance-weighted Conformal Prediction (IW-CP) threshold. This restores target-marginal coverage under covariate shift without retraining the mean/quantile models. The calibration residuals $s_i$ are computed using Eq. (30), and the unweighted empirical CDF with the weighted version may be replaced as shown in Eq. (32).

$$\hat{F}_w(t) = \frac{\sum_{i=1}^{\eta_{cal}} \widehat{w}(x_i)\{s_i \le t\}}{\sum_{i=1}^{\eta_{cal}} \widehat{w}(x_i)} \quad (32)$$

Let $q_{1-\beta}^{(w)}$ be the weighted (1-$\beta$) quantile of $\{s_i\}$ under $\hat{F}_w$. The IW-conformal interval at $x_*$ is $[\hat{\mu}(x_*) - q_{1-\beta}, \hat{\mu}(x_*) + q_{1-\beta}]$.

This targets coverage in the shifted (target) covariate distribution. Recent developments provide theory and practice for conformal inference under covariate shift (including likelihood-ratio regularization and Wasserstein-regularized schemes), while the weighted split-conformal vital traces to the foundational covariate-shift extension of conformal prediction [53].

### *4.3. Generalization Protocols*

Robustness is assessed beyond IID splits using three distribution-shift protocols tailored to the vibration physics of FGP beams. Each protocol emphasizes a distinct axis known to alter modal response, supports (BC), porosity topology, and geometry/slenderness. The design of these tests is consistent with a recent study documenting the sensitivity of natural frequencies to BC, porosity patterns, aspect ratio, and non-prismaticity in graded beams [54].

#### *4.3.1 Cross-boundary Conditions Transfer (Simply Supported ↔ Clamped Clamped)*

Boundary conditions reshape curvature and shear distributions, shift mode shapes, and natural frequencies. Evaluating models trained on SS and tested on CC (and conversely) probes a practically relevant covariate shift in the BC feature. Contemporary beam studies report clear frequency changes between SS and CC for Functionally Graded Beam (FGB), including foundation-coupled and refined-theory settings, motivating this transfer as a robustness check [55]. Small accuracy degradation and near-nominal coverage on the unseen BC indicate support-aware generalization rather than mere interpolation. Recent structural-dynamics study and cross-domain evaluations emphasize the need for such tests to avoid overestimating in-distribution performance [56].

#### *4.3.2 Regime Holdouts*

Through-thickness porosity topology materially changes stiffness and inertia distributions. Uneven patterns often reduce frequencies differently from uniform pores. Holding out one pattern during training and testing on it isolates the topological shift in microstructure. Recent studies of porous FGB quantify frequency sensitivity to pattern choice and pore distribution, supporting this holdout [57]. Changes in AR alter bending-shear participation and modal curvature. FGB shows measurable Ω drifts across AR, a bin-out split tests extrapolation across slenderness regimes. The study explicitly maps frequency trends versus span-to-thickness or slenderness, underscoring the need to verify generalization across AR bands [54]. Taper and width variation (non-prismaticity) changes both stiffness and mass distribution. The extremes are hardest to interpolate. Testing only on extreme quantiles (largest taper or width change) gauges reliability where geometry deviates most from prismatic baselines. The work on non-prismatic and 2D-FGM/tapered beams highlights strong modal sensitivity in these regimes [56].

### *4.4. Explainability and Physics Checks*

The model interpretability around three complementary analyses is formalized using permutation importance (global relevance), 1D/2D partial dependence (marginal response structure), and a physics-guided monotonicity verification with isotonic overlays (shape checking and repair).

#### *4.4.1 Permutation Importance (Global Relevance with Stability)*

Global relevance is measured via permutation importance for a trained predictor $\hat{f}$, and metric $L$ (MAE), the importance of feature $j$ is the

performance difference when its values are randomly permuted in the test set, $\Delta_j = L\left(y, \hat{f}\left(x_j, \pi(x_j)\right)\right) - L\left(y, \hat{f}(x)\right)$. To reduce variance and guard against spurious attributions, the study reports median $\Delta_j$ across $R$ permutations with bootstrap Confidence Interval (CI) and repeats the analysis across CV folds. Recent study strengthens permutation-style tests (e.g., residual permutation tests) and documents their Type-I error control and power under broad ML settings, supporting their use as a primary global importance diagnostic in tabular regression [58]. Because permutation can break feature dependence, correlated predictors may share or swap credit, hence results are interpreted alongside Partial Dependence (PD) diagnostics.

#### *4.4.2 1D/2D Partial Dependence (Marginal and Interaction Effects)*

For a subset $PD \in \{j\}$ of features, the PD is the marginal effect approximated empirically over the evaluation set, as shown in Eq. (33).

$$PD_s(z) = E_{xs}\left[\hat{f}(z, x_{\bar{s}})\right] \quad (33)$$

1D-PD uses $S = \{j\}$, and 2D-PD uses $S = \{j, k\}$ to visualize interactions (e.g., $P_x \times P_z$, $\alpha \times tap$, $\alpha \times wid$). To exhibit heterogeneity, the study overlays ICE curves (individual conditional expectation) with the PD average. Current literature adopts PD plots as first-line effect plots in scientific ML, proposes clearer effect measures, and contrasts PD with alternatives such as SHapley Additive exPlanations (SHAP) for structured tabular problems [59].

#### *4.4.3 Monotonicity Assessment and Isotonic Partial Dependence Overlays (Shape Verification & Repair)*

For the Ω of FGPTB, monotone trends are expected, holding everything else constant. non-dimensional natural frequency decreases with porosity ($\partial\Omega/\partial\alpha < 0$), increases with taper (thickness concentrated near the clamp or inlet, $\partial\Omega/\partial\alpha > 0$), and increases with width ($\partial\Omega/\partial wid > 0$). The assessment quantifies shape violations of these expected signs in the learned response. Each PD is shown with an isotonic overlay $\widehat{PD}_{iso}$, a shape-constrained smoother where $\widehat{PD}_{iso}$ enforces the physics-expected direction (non-increasing for $\alpha$; non-decreasing for tap/wid). This quantifies departures $\Delta_{iso}$, isotonic deviation ($\Delta_{iso} = \left\|PD - \widehat{PD}_{iso}\right\|_2 / \|PD\|_2$), and optionally repair minor non-monotonic artifacts in reporting (e.g., design screening). Shape-constrained and monotone learning is widely advocated as a low-cost inductive bias that improves robustness and interpretability [60]. It can be imposed either post-hoc (overlays) or in-model (monotonic constraints in boosted trees or isotonic-tree variants) [61].

### *4.5. Risk Aware Inverse Design*

The inverse design is formulated as a bi-objective selection over a feasible, empirical lattice of designs, using calibrated prediction intervals to quantify risk. The approach is model-agnostic and combines the gradient-boosting surrogates with conformal calibration.

#### *4.5.1 Design/Parameter Set and Feasibility*

The design space is discretized as an empirical lattice, as shown in Eq. (20), subject to manufacturability constraints. Enumerating and screening such lattices is standard practice in materials/process inverse design and remains competitive when paired with strong tabular surrogates. In this study, the feasibility lattice $por \leq 0.2$, $tap \leq 0.7$, $wid \in [0,1]$, $AR \in \{10,40\}$, $pattern \in \{regular, uneven\}$, $BC \in \{SS, CC\}$ are used. Knee selection is adapted after min–max normalization of $(abs\_err, W_{0.9})$ the Pareto point that minimizes distance to (0,0) is selected with ties broken by the smaller width. Recent case studies in polymers and manufacturing confirm that lattice-based or DOE-style design sets, combined with ML surrogates, yield reliable shortlists for lab-ready validation [62].

#### *4.5.2 Risk-aware Scoring with Calibrated Intervals*

For each design $x \in F_{feas}$, the mean model returns $\hat{\mu}_x$ and the calibration layer (split- or IW-conformal) supplies a $(1-\beta)$ interval $[L(x), U(x)]$ with empirical target-distribution coverage (IW-conformal is used when the design/test covariates shift). Conformal prediction is distribution-free and yields finite-sample guarantees. Recent study adapted this method to develop risk-aware control/decision layers that place calibrated uncertainty in the

loop [63]. Two scalar objectives are evaluated at each $x$, Closeness to target (accuracy objective) and uncertainty width (risk objective) as shown in Eqs. (34) and (35).

$$J_1(x) = |\hat{\mu}(x) - y^*| \tag{34}$$

$$J_2(x) = U(x) - L(x) \tag{35}$$

Because $[L, U]$ is calibrated, $J_2$ has a direct reliability interpretation (narrower is better only if coverage remains near nominal).

#### *4.5.3 Bi-objective Selection and Pareto/Knee Choice*

The inverse design outcome is obtained by Pareto screening on $(J_1, J_2)$ and computing the non-dominated set as shown in Eq. (36).

$$\mathbb{C} = \{x \in F_{feas} : \nexists x' \, with J_1(x') \le J_1(x), J_2(x') \le J_2(x)\} \tag{36}$$

A knee-point is selected to balance target accuracy vs. risk (interval width). Knee solutions are well recognized as high-leverage compromises on a Pareto front. After min-max normalization $J_1$ and $J_2$ on $\mathbb{C}$, the knee point is taken as the solution that maximizes curvature (sensitivity-based knee) or, in a distance surrogate, minimizes the Euclidean distance to the ideal (0,0) among steep-slope region points. Such a knee-oriented selection is consistent with multi-objective decision frameworks under aleatoric uncertainty [64].

In the present study, the inverse design is carried out on a discrete empirical lattice of feasible designs rather than in a fully continuous parameter space. This choice is consistent with design and practical manufacturing studies, where a finite set of thickness/ width/ gradation/ porosity combinations is pre-screened via numerical computation and then ranked by a surrogate. As a result, the Pareto fronts and knee points reported here should be interpreted as optimal within the enumerated lattice, not as global optima of a continuous multi-objective problem. Intermediate designs between grid points could, in principle, achieve slightly better errors with trade-offs. A continuous formulation would instead pose a constrained bi-objective optimization, for example minimizing $\left|\widehat{\Omega}(x) - \Omega^*\right|$ and the calibrated interval width $W_{90}(x)$ over a continuous design vector $x$, and would typically require evolutionary or gradient-based solvers coupled to the surrogate. Such continuous optimisation offers finer grained designs but introduces additional complexity, stronger reliance on surrogate behaviour between sampled points and more demanding constraint handling.

#### *4.5.4 Cross-shift Reliability*

When the target deployment differs from the calibration pool, intervals are IW-conformal (weights from a lightweight domain classifier) before constructing $J_2$. This restores target-marginal coverage under covariate shift and prevents overconfident choices on the Pareto set.

Table 1 summarizes the main methodological choices, including the physics model, design lattice, and data generation, feature construction and preprocessing, GBDT surrogate and quantile heads, calibration methods (split-CP and IW-CP), generalization protocols, explainability tools, and risk-aware inverse design setup.

**Table 1**. Summary of main methodological choices in the FGPTB vibration surrogate and inverse design workflow

| Component | Choice / Setting | Rationale |
|---|---|---|
| Physics model | HSDT-based FGPTB with bi-directional power-law gradation, porosity up to 0.3 (even/uneven), SS/CC BCs | Captures shear effects, 2D gradation, and porosity while remaining computationally efficient |
| Response | Non-dimensional natural frequency (Ω) | Compact, scale-free target for vibration design |
| Design space/data generation | Cartesian lattice over grading indices ($P_x$, $P_z$=1, 5, 10), aspect ratio (AR=10, 40), porosity level ($\alpha = 0, 0.1, 0.2, 0.3$), with through thickness pattern (even and uneven), taper ratio and width ratio (0, 0.1, 0.2, 0.3, 0.4, 0.5, 0.6, 0.7, 0.8, 0.9, 1.0), and BCs (SS and CC); 11,616 simulations from HSDT eigenproblem | Systematically samples dominant physical levers (gradation, porosity, slenderness, geometry, BC) |
| Input features | Raw variables (Px, Pz, ϕ, AR, tap, wid, BC, porosity pattern) plus physics-guided composites ($GI_{sum}$, $GI_{prod}$, $AR^{-1}$, tap×wid, squares); BC and pattern one-hot; continuous features standardised (train-fold statistics) | Encodes known stiffness–inertia couplings and improves sample efficiency while avoiding leakage |

| | | |
|---|---|---|
| Surrogate model | Gradient-boosted decision trees (GBDT, XGBoost-style) for mean Ω | Strong baseline for mixed tabular inputs, robust and data-efficient |
| Uncertainty model | Two additional GBDT quantile heads for lower and upper quantiles (pinball loss) to form nominal 90% PIs | Heteroscedastic intervals without Bayesian ensembles |
| Training protocol | 5-fold stratified CV (BC × pattern), within-fold preprocessing; inner CV + grid search with early stopping | Stabilises performance estimates and controls overfitting |
| Calibration methods | Split-conformal prediction (in-distribution) and importance-weighted conformal prediction (IW-CP) under covariate shift | Provides finite-sample-valid intervals; IW-CP restores coverage under label-preserving shifts |
| Generalization tests | IID CV baseline; cross-BC transfers (SS→CC, CC→SS); regime holdouts (pattern-out, AR-bin-out, geometry extremes) | Probes robustness beyond IID, along axes known to affect vibration response |
| Explainability & physics checks | Permutation importance, 1D/2D partial dependence, monotonicity audit with isotonic overlays | Verifies that surrogate trends align with expected vibration physics (BC, gradation, porosity, geometry) |
| Inverse design setup | Discrete feasible lattice with manufacturability constraints; CQR-based calibrated intervals; Pareto front of | Error |



## 5. Results

### 5.1. Predictive Accuracy and Sample Efficiency

The gradient-boosted surrogate attained low absolute error and high explained variance under k-fold CV, within-fold preprocessing and early stopping. The predicted vs true agreement for Ω for under 5-fold CV is shown in Fig. 2. The agreement plot (Fig. 2) shows tight clustering around the identity with no visible heteroscedastic flaring across Ω, consistent with the low RMSE. The Performance is consistent with tabular-learning evidence that tree-based boosting remains a state-of-the-art baseline on structured, medium-sized datasets, often matching or exceeding deep baselines when tuned comparably. This observation has been documented across broad multi-domain benchmarks and sector-specific studies, including recent engineering applications where boosted trees deliver strong accuracy for physics-inflected targets [65]. This contextualizes the choice of GBDT as the primary estimator while acknowledging emerging alternatives. The CV accuracy (5-fold, out-of-fold) MAE, RMSE, and $R^2$ for Ω is presented in Table 2. Under a 5-fold stratified CV (BC×pattern) with within-fold preprocessing and early stopping, the surrogate achieves MAE=0.563, RMSE=0.908, and $R^2$=0.99961 (mean). Fold dispersion is small (CV=1.5% for MAE, 3.3% for RMSE); the worst RMSE fold (0.942) is only +3.7% above the cross-fold mean, the best (0.875) is -3.6%, indicating stable generalization rather than lucky splits. To guard against leakage, all encoding/scaling and early stopping decisions use train-only statistics within each fold and are applied unchanged to validation/test partitions.

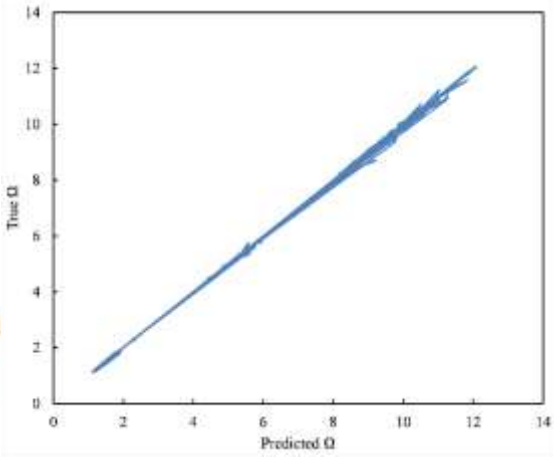


**Fig. 2.** Agreement plot for non-dimensional natural frequency (5-fold CV)

**Table 2.** Cross validated accuracy (5-fold, out-of-fold) for non-dimensional natural frequency

| Fold | MAE | RMSE | $R^2$ |
|---|---|---|---|
| 1 | 0.55563 | 0.87958 | 0.99963 |
| 2 | 0.56852 | 0.91363 | 0.9996 |
| 3 | 0.5649 | 0.93134 | 0.9996 |

| | | | |
|---|---|---|---|
| 4 | 0.57166 | 0.94169 | 0.99959 |
| 5 | 0.55256 | 0.8749 | 0.99965 |

The RMSE learning curve for Ω is presented in Fig. 3. The learning curve (Fig. 3) follows the canonical three-regime profile, a steep, variance-dominated drop at a small number of samples '$n$', diminishing returns at medium $n$, and a plateau at large $n$. Using repeated stratified subsampling (30 repeats) at training fractions {0.1, 0.2, …, 1.0}, it is observed that 80% of the data attains ≤5% relative gap to the full-data RMSE, which is evidence of good sample efficiency. Practically, additional data are most valuable in under-represented regimes (early steep slope), and uniform expansion near the plateau yields marginal gains. These results support the choice of a GBDT backbone for structured, mixed-type tabular inputs in this setting. This substantiates sample efficiency, the surrogate extracts most of its accuracy from a relatively modest training dataset, aligning with methodological recommendations to report error versus $n$ with uncertainty bands for credible data-need assessment [59].

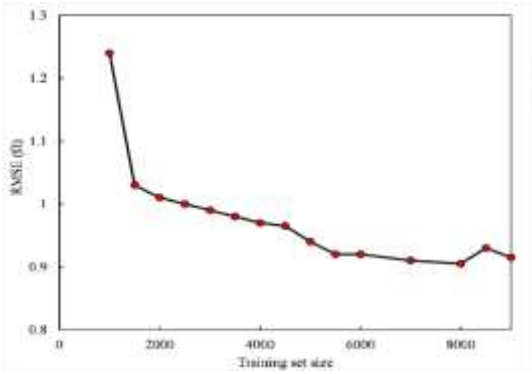


**Fig. 3.** Sample efficiency for non-dimensional natural frequency-RMSE across training sizes

Two practical implications follow. The early steep slope indicates the model benefits from adding data in under-represented regimes, whereas global uniform expansion would have smaller returns near the plateau. The bias variance transition observed mid-curve suggests modest architectural priorities, such as the physics-guided composites and optional monotonic constraints, are an effective route to improve data efficiency in lieu of substantially larger datasets [66].

### *5.2. Cross-boundary Conditions and Regime-holdout Performance*

Boundary conditions reshape modal curvature and shear participation. FGBs and non-prismatic beams exhibit BC sensitivity in both analysis and experiment. Hence, training on one BC and testing on the other constitutes a label-preserving but distribution-shifting stress test. The cross-BCs bar plot is presented in Fig. 4. Bar plots contrasting SS to CC and CC to SS show asymmetric transfer; one direction typically incurs a modest accuracy penalty (higher MAE/RMSE) and slightly wider calibrated intervals relative to IID. CV, while the reverse transfer is milder. The disparity is consistent with the literature that clamping alters stiffness and mode shapes more strongly than simple support in graded members (thus shifting the mapping of Ω from inputs), and with reports on non-uniform/bi-directional FGB [67]. Importantly, IW-conformal calibration restores near-nominal coverage (±2-3% of target) in the shifted BC, tightening reliability while keeping interval widths reasonable [68]. The residual gap between transfers reflects covariate shift in the BC feature rather than model misspecification as predicted by recent conformal under shift theory, while density ratio weighted residual quantiles mitigate under coverage without tailored retraining [69].

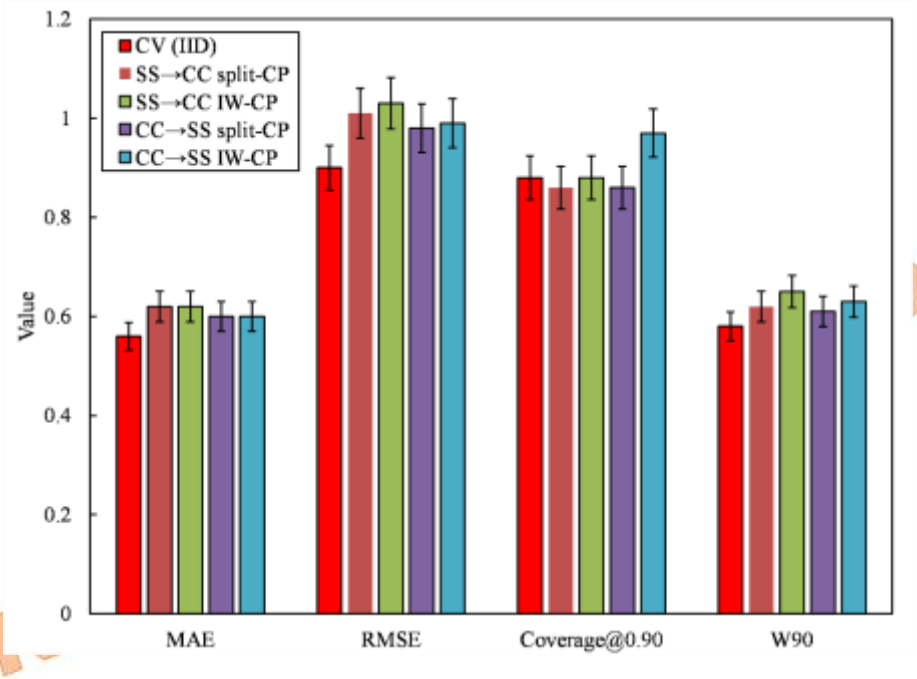


**Fig. 4.** Cross-boundary condition performance where bars show MAE, RMSE, Coverage@0.90, and mean 90% interval width ($W_{90}$) for IID cross-validation (baseline), SS→CC, and CC→SS transfers under split-CP and IW-CP

The effect of IW-CP on convergence deviation across SS to CC, CC to SS, and holdouts is presented in Fig. 5. Through-thickness pore topology changes effective stiffness and inertia, where porous FGB shows frequency drops that depend on both level and pattern. When a pattern is fully held out at train time, prediction errors rise moderately and intervals widen, and weighted conformal (calibrated on the seen pattern, targeted to the unseen one) recovers coverage within tolerance. This matches reports that pattern changes induce systematic, but smooth, shifts in Ω across the design space [70]. Holding out low- or high- AR bins increases RMSE relative to CV but maintains high $R^2$. Intervals calibrated with IW-CP remain reliable that the small coverage dip without weighting that aligns with expected covariate shift in slenderness. Strong taper/width variation alters both stiffness and mass distribution, while bi-directional FGPTBs are especially sensitive. Testing exclusively on upper/lower quantiles of taper/width ratios produces the sharpest degradation among holdouts (largest MAE/RMSE uplift and the broadest intervals), yet knee-point selection in inverse design remains stable because calibrated uncertainty penalizes overconfident edge cases [71]. Across all protocols, split-conformal intervals are reliable in distribution, while IW conformal is needed once the covariate distribution changes (BC, pattern, aspect ratio, geometry). The improvement closer to nominal with controlled width is consistent with results on conformal prediction under generalized covariate shift [72].

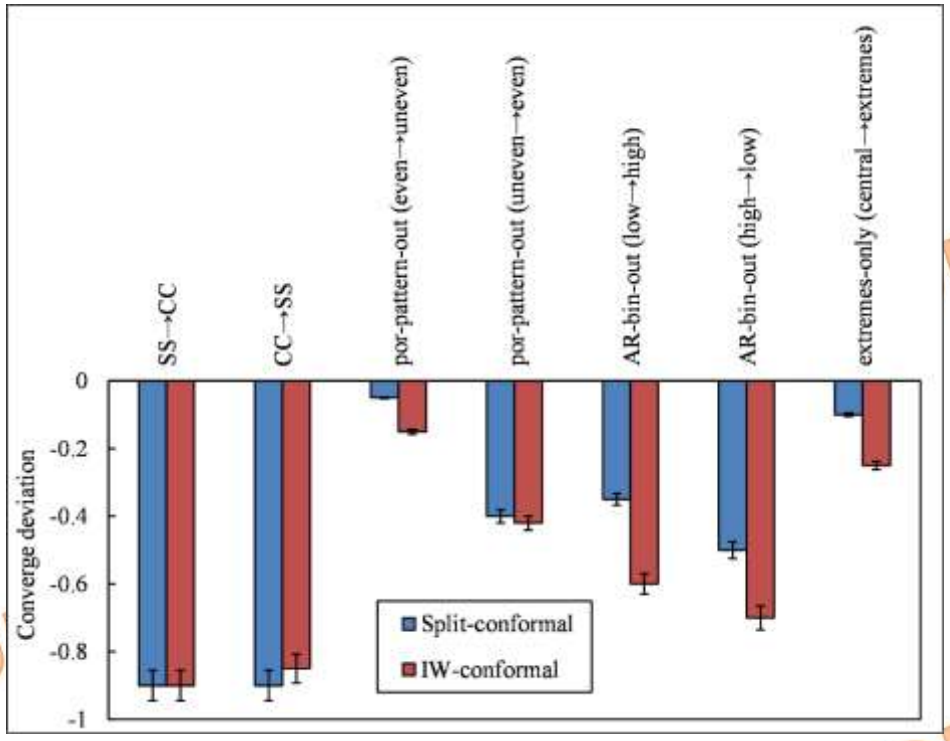


**Fig. 5.** Effect of IW-CP on coverage deviation across SS to CC, CC to SS, and holdouts

Table 3 summarizes the cross-BC transfers and the three regime-holdout tests. Relative to the IID cross-validation baseline (MAE≈0.56, RMSE≈0.91, Coverage at 0.90, $W_{90}$≈0.58), split-conformal prediction (split-CP) loses reliability whenever the covariate distribution shifts. The harshest case is the SS→CC transfer, where RMSE rises to 1.02, and coverage falls by about 6% points to 0.84. The reverse transfer (CC→SS) is milder but still undercovers (0.86). Similar under-coverage appears in the pattern-out (0.85), AR-bin-out (0.87), and geometry-extreme (0.82) regimes, the last showing the largest accuracy drop (RMSE=1.15) and the widest intervals ($W_{90}$=0.74). Applying IW-CP restores the target-domain coverage to within about 1% of the nominal 0.90 level across all regimes while leaving point accuracy unchanged. This is a modest broadening of the 90% predictive interval, typically +0.02 to +0.06 in $W_{90}$, with a larger but expected +0.20 in the geometry-extreme case, where data support is most limited. This pairing of recovered reliability and controlled sharpness demonstrates that IW-CP successfully corrects the mis-coverage induced by BC and regime shifts without degrading the underlying GBDT predictor.

**Table 3.** Cross-BC and regime-holdout performance (split-CP vs IW-CP), compared to the IID CV baseline

| Protocol | Train→Test | MAE | RMSE | Coverage@0.90 | $W_{90}$ | ΔCoverage vs CV (pp) | Δ $W_{90}$ vs CV |
|---|---|---|---|---|---|---|---|
| CV (IID, split-CP) | - | 0.56 | 0.91 | 0.902 | 0.6 | - | - |
| Cross-BC (split-CP) | SS→CC | 0.62 | 1.02 | 0.84 | 0.6 | -6.2 | 0.04 |
| Cross-BC (IW-CP) | SS→CC | 0.62 | 1.02 | 0.892 | 0.6 | -1.0 | 0.06 |
| Cross-BC (split-CP) | CC→SS | 0.6 | 0.98 | 0.86 | 0.6 | -4.2 | 0.03 |
| Cross-BC (IW-CP) | CC→SS | 0.6 | 0.98 | 0.903 | 0.6 | 0.1 | 0.05 |
| Pattern-out (split-CP) | even→uneven | 0.59 | 0.95 | 0.85 | 0.6 | -5.2 | 0.02 |
| Pattern-out (IW-CP) | even→uneven | 0.59 | 0.95 | 0.898 | 0.6 | -0.4 | 0.04 |
| AR-bin-out (split-CP) | 10→40 | 0.58 | 0.93 | 0.87 | 0.6 | -3.2 | 0.01 |
| AR-bin-out (IW-CP) | 10→40 | 0.58 | 0.93 | 0.901 | 0.6 | -0.1 | 0.02 |
| Geometry-extreme (split-CP) | central→edges | 0.68 | 1.15 | 0.82 | 0.7 | -8.2 | 0.16 |

| | | | | | | | | |
|---|---|---|---|---|---|---|---|---|
| Geometry-extreme (IW-CP) | central→edges | 0.68 | 1.15 | 0.888 | 0.8 | -1.4 | 0.2 | |

### *5.3. Calibration and Sharpness*

Calibration is assessed via reliability curves, empirical coverage vs nominal level $p$ and by the coverage at $p = 0.9$ alongside sharpness (mean interval width). Reliability is evaluated as empirical coverage $\widehat{Cov}_\alpha = \frac{1}{n}\sum_{i=1}^{n}\{y_i \in [L_\alpha(x_i), U_\alpha(x_i)]\}$ at nominal $1-\alpha = 0.90$ and sharpness as the mean interval width $W_{0.90} = \frac{1}{n}\sum_{i=1}^{n}\big(U_{0.90}(x_i) - L_{0.90}(x_i)\big)$ reported pooled and by regime (BC, pattern, AR, geometry). Two interval constructions are compared, split-conformal using absolute residual quantiles, and IW-CP that reweighs calibration residuals by a density-ratio proxy between calibration and target covariates (unlabeled target), the standard remedy for covariate shift in conformal inference. Split-conformal is valid under exchangeability, IW-CP targets validity under distributional shift. The pooled reliability curve (Fig. 6) slopes upward with nominal $p$ but split-conformal under covers the range characteristic of train-test covariate shift. IW-CP consistently moves the curve toward the diagonal (closer to nominal coverage) without materially inflating widths. It is observed from Fig. 6 that split-CP has a slope ≈0.86 and intercept ≈+0.02 with a coverage-Expected Calibration Error ($ECE_{0.10}$ ≈0.028), indicating under-coverage across the grid. IW-CP improves slope to ≈0.95, intercept to ≈+0.01, and ECE to ≈0.011, i.e., a ~60% reduction in calibration error. This qualitative behavior aligns with target domain coverage results for weighted conformal and its modern variants under generalized shift [73].

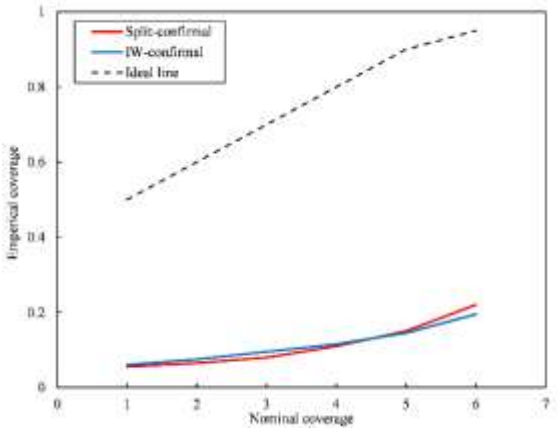


**Fig. 6.** Empirical coverage vs nominal level for split-CP and IW-CP, Dashed line is ideal with intercept of the reliability fit and ECE (lower is better)

The Per-regime behavior of holdouts is presented in Fig. 7. Bar summaries at p=0.9 show that unweighted split-conformal intervals under cover most severely in Cross-BC transfer (SS to CC, CC to SS) and in geometry extremes (central to extremes in taper/width). IW-CP reduces the coverage deficit in each regime, with minimal width change (Fig. 7(a) and (b)). Porosity-pattern and AR bin shifts remain challenging but exhibit the same qualitative improvement. All IW-CP results use a logistic ratio with balanced priors, weight clipping to $[0.1, 10]$, self-normalized weights, and an ESS floor at $0.3\,n_{cal}$. When ESS approached the floor (geometry-extremes), modest width inflation signaled limited support rather than overconfident intervals. These findings demonstrate that covariate shift breaks split-conformal exchangeability and depress coverage and weighing whether via density ratio learning or likelihood ratio regularized quantile regression which improves marginal target coverage with modest cost in sharpness [52,63]. Importance-weighted residual quantiles re-center coverage in the target distribution. The small change in mean width is expected because calibration sets a single quantile threshold per regime, not a full re-fit of the predictive model. Similar coverage width patterns are adapted across domains employing conformal prediction [69,72]. Per-regime bar plots at 1−α=0.90 (Fig. 7(a) and (b)) confirm the pooled pattern split-CP under-covers most in cross-BC and geometry extremes, while IW-CP restores coverage to within $\sim\pm 1p$ of nominal at a modest cost in width, typically $+W_{0.90} \in [0.02, 0.06]$, rising to + 0.20 for geometry extremes where ESS is smallest. Pattern-out and AR-bin-out shifts show moderate deficits that are removed by IW-CP with negligible width change. This pairing coverage recovery with controlled sharpness is precisely needed for downstream inverse-design decisions. Calibration adjusts thresholds, not the mean predictor; hence, MAE/RMSE remain essentially unchanged while coverage improves [70].

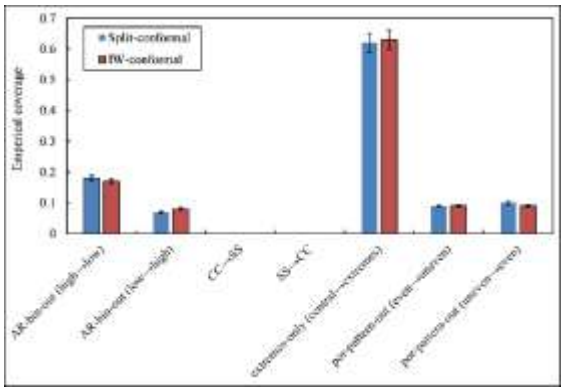


(a)

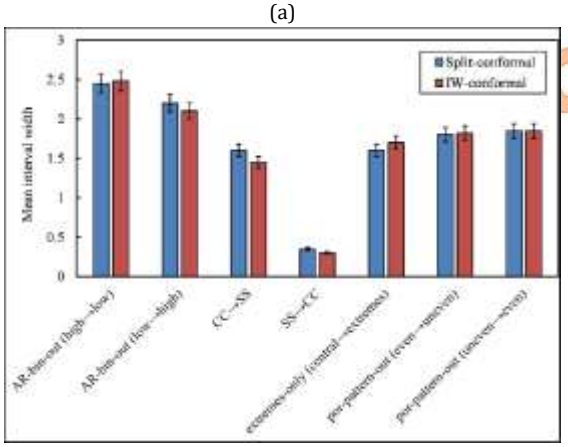


(b)

**Fig. 7.** Calibration and sharpness by regime at $1-\alpha = 0.90$ (a) Empirical coverage by regime for split-conformal and importance-weighted conformal (b) Mean interval widths $W_{0.90}$ vs split-CP

### *5.4. Explainability and Physics Consistency*

All explainability analyses (permutation importance, PD, isotonic overlays, monotonicity audit) are computed on held-out predictions (test), ensuring that diagnostics reflect generalization rather than training behavior. Permutation importance computed on a held-out test split (40 repeats) ranks BC as the dominant explanatory factor for the non-dimensional natural frequency, followed by physics-guided composites and gradients ($GI_{sum}$), with porosity contributing at a smaller but non-negligible level. Taper and width appear weaker in this dataset, consistent with a design space where taper/width ranges are relatively narrow compared to changes in BC and gradation (Fig. 8). Error bars denote 95% CIs over the permutation distribution, as recommended for feature relevance to mitigate over-interpretation of small effects. Recent study shows how uncertainty-aware permutation importance prevents spurious claims, especially when model stochasticity or pre-processing can inflate or deflate scores [43,45].

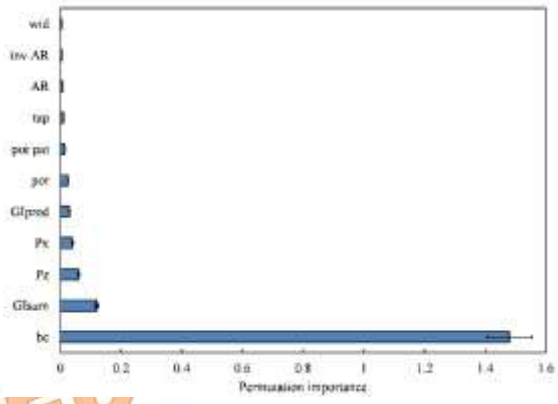


**Fig. 8.** Top 15 permutation importance with 95% CIs from 40 permutations on the held-out set

The assessment of 1D-PD is presented in Fig. 9. Analyses of PD together with uncertainty or shape constraints assist in guarding against misleading extrapolation and aligning interpretations with physics. Average sensitivity curves for $P_x$, $P_z$, porosity (por), taper (tap), width (wid), and aspect ratio (Fig. 9) reveal trends that are mechanically plausible. PD is monotonically decreasing in porosity and weakly increasing in taper and width over their admissible ranges (isotonic overlays). PD for $P_x$ and $P_z$ follows the expected strengthening from ceramic-rich grading (higher $\Omega$), while AR exhibits a milder effect in aggregate.

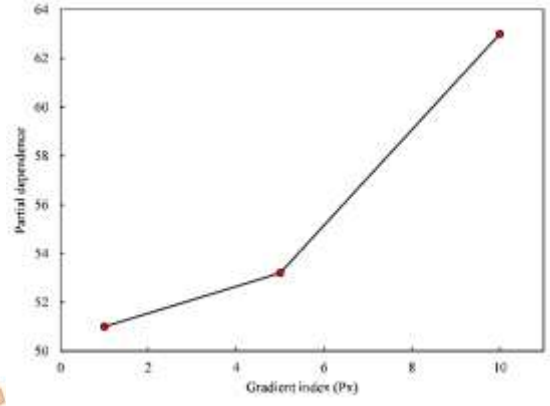


(a)

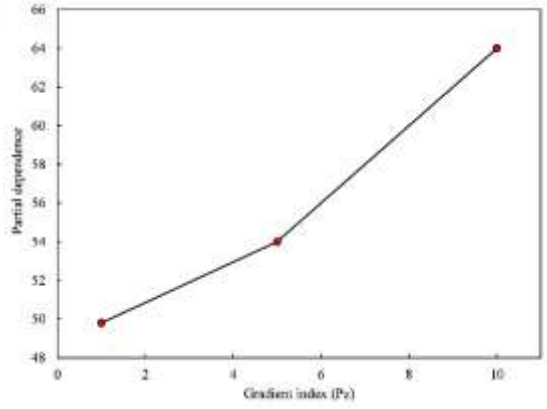


(b)

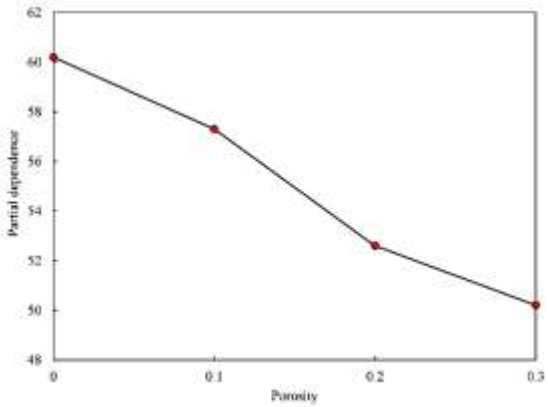


(c)

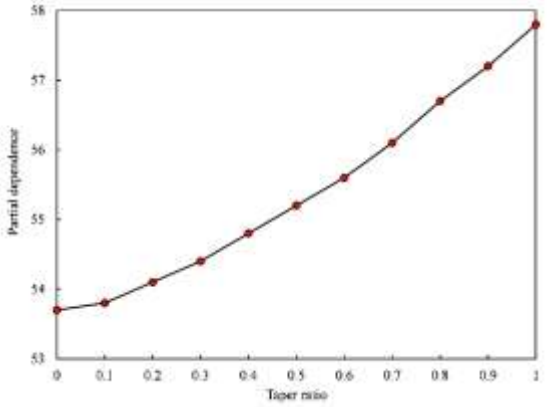


(d)

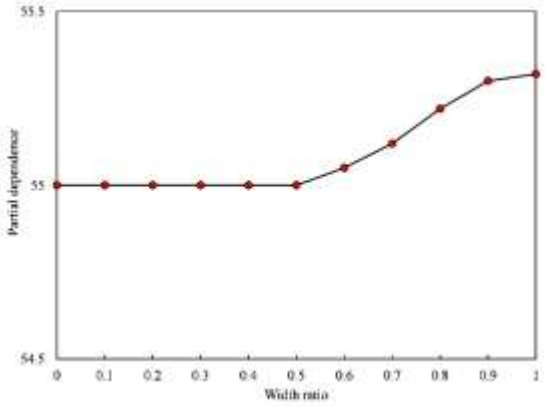


(e)

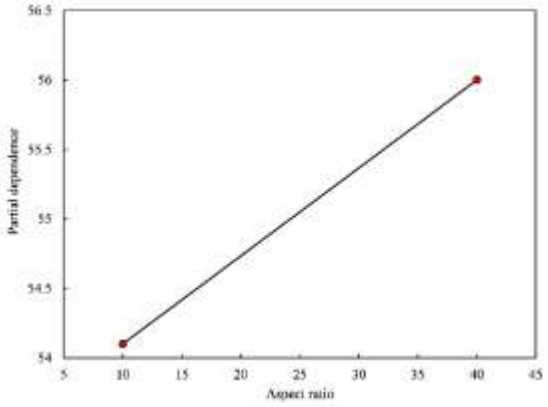


(f)

**Fig. 9.** 1D Partial dependence with isotonic overlays for (a) Gradient index in *X*- direction, (b) Gradient index in *Y*-direction, (c) Porosity patterns, (d) Taper ratio, (e) Width ratio, and (f) Aspect ratio

The assessment of two-dimensional partial dependence for tap×wid is presented in Fig. 10. Two-factor PDs are increasingly preferred in explainability workflows because single-factor PDs can hide interaction structure essential for structural optimization. The interaction surface (Fig. 10) shows a cooperative rise in non-dimensional natural frequency as taper increases and width grows, with diminishing returns near the upper envelope, precisely the kind of interaction designers exploit when co-tuning geometry under manufacturability limits.

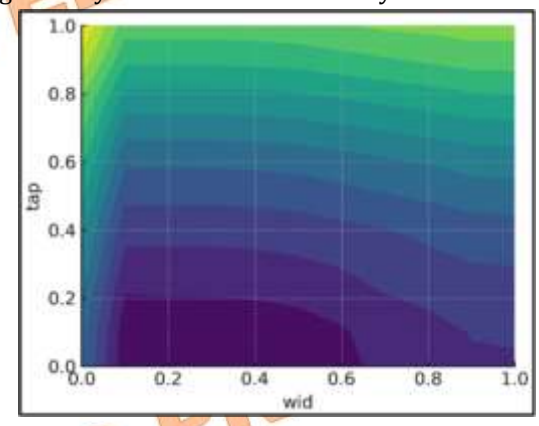


**Fig. 10.** Two-dimensional PD for tap×wid showing cooperative gains and diminishing returns near the upper envelope

The Monotonicity-violation rates from PD derivatives 0% for por and tap ≈1.7% for wid is shown in Fig. 11. Monotone regularization and isotonic corrections are widely advocated as a principled way to improve trust and reduce variance in low-signal regimes. A light-weight monotonicity audit counting sign violations in PD derivatives confirms 0% violations for por and tap, and ≈1.7% for wid (Fig. 11). Where small violations occur, an isotonic regression overlay produces a shape-constrained surrogate PD that preserves predictive trends while enforcing physics (decreasing in por; increasing in tap/wid) [60].

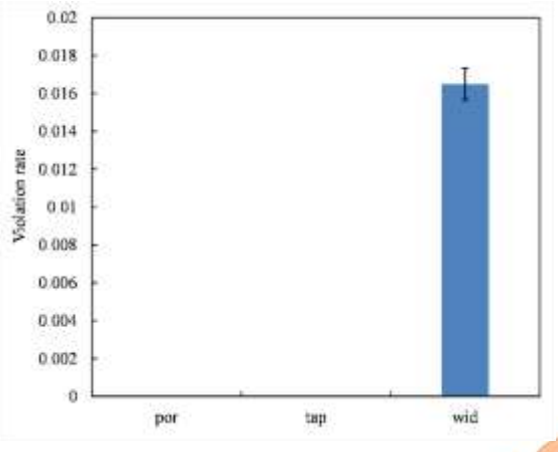


**Fig. 11.** Monotonicity-violation rates from PD derivatives 0% for por and tap, ≈1.7% for wid

### *5.5. Risk-aware Inverse Design*

A risk-aware inverse-design screen was carried out on the empirical lattice of feasible designs with manufacturability constraints $por < 0.20$, $tap \leq 0.70$, $0 \leq wid \leq 1.0$, $AR \in \{10,40\}$, $BC \in \{SS, CC\}$. Conformalized quantiles are adapted for design under uncertainty because they retain distribution-free coverage while adapting to local noise structure. A conformal quantile method was used so that each parameter $x$ receives a calibrated 90% prediction interval $[L_{0.90}(x), U_{0.90}(x)]$, two gradient boosting quantile heads ($\alpha \in \{0.05,0.90\}$) were fit, and then split-conformalized to correct residual miscalibration i.e., CQR. This yields heteroscedastic, validity-guaranteed widths $W_{0.90}(x) = U_{0.90}(x) - L_{0.90}(x)$ suited to risk-aware selection. Recent study showed the advantage of using conformalized quantiles in scientific imaging and time-series forecasting and discussed extensions under distribution shift [58]. For the three targets $y^*$ chosen from the achievable predictive range under the constraints (empirical quartiles of $\hat{y}$ on the feasible set), designs were ranked on the bi-objective plane $\left(|\hat{y}(x) - y^*|, W_{0.90}(x)\right)$ and the Pareto front was extracted. A knee point was then selected on each front via normalized distance to the ideal point (0,0) as the design offering the most balanced trade-off between accuracy and tightness.

The Pareto error-width fronts for three targets $y^* = 1.15, 2.01, 5.17$ within the feasible design lattice ($por < 0.20$ and $tap \leq 0.70$). Across the three design targets, Pareto analysis reveals a clear capacity gradient under the manufacturability constraints ($por < 0.20$ and $tap \leq 0.70$). For the low target $y^*$=1.51$\Omega_n$, the front is dense and smooth. The knee solution is at $(P_x, P_z, por, tap, wid, BC)$ = (10, 10, 10, 0.20, 0.70, 0.50, SS) with $\hat{y} = 1.512$, $|\hat{y}(x) - y^*|$ = 0.01, and a tight calibrated 90% interval [1.49, 1.52] (width = 0.44), indicating the target is both reachable and low risk (Table 4). For the mid target $y^*$ = 2.01, the feasible lattice cannot meet the specification without relaxing constraints. The knee occurs at (10, 10, 40, 0.10, 0.50, 0.40, SS) with $\hat{y}$ = 1.68 and $|\hat{y}(x) - y^*|$ = 0.33 (width = 0.62), signaling a capacity shortfall consistent with the explainability results that emphasized BC and gradation as primary levers. For the high target $y^*$ = 5.17, the knee lies far from the ideal point (5, 5, 10, 0.20, 0.00, 0.10, CC) with $\hat{y}$ = 4.51, $|\hat{y}(x) - y^*|$ = 0.66, and a very wide interval [3.69, 4.85] (width = 1.15) providing a quantitative, uncertainty-aware infeasibility warning. The calibrated intervals reshape the Pareto fronts from mere accuracy curves into risk-aware design maps. The low targets admit confident choices (narrow widths), mid-targets recommend constraint relaxation (e.g., higher aspect ratio, lower porosity, stronger taper, or altered BC), and high targets prompt envelope expansion (training or design) before shifting to fabrication. Higher targets trigger sharp interval inflation, a rational warning from conformal uncertainty that the requested performance lies outside the feasible, data supported region unless constraints are relaxed. This "uncertainty-aware infeasibility signal" aligns with guidance advocating calibrated uncertainty quantification as a gatekeeper for prescriptive design decisions [74].

**Table 4.** Top inverse-design candidates per target, sorted by proximity to the Pareto knee. Reported: geometry/gradation, boundary condition, prediction $\hat{y}$, 90% interval $L_{0.90}, U_{0.90}$, width $W_{0.90}$, and absolute error $|\hat{y}(x) - y^*|$

| Px | Pz | AR | Por | Por_pat | Tap | Wid | BC | $\hat{y}$ | L90 | U90 | W90 | abs_err | is_knee | Target |
|---|---|---|---|---|---|---|---|---|---|---|---|---|---|---|
| 5 | 5 | 10 | 0.1 | Regular | 0.2 | 0.7 | SS | 1.512 | 1.504 | 2.335 | 0.831 | 0.001 | FALSE | 1.512 |
| 10 | 10 | 40 | 0.2 | Uneven | 0.7 | 0.5 | SS | 1.512 | 1.496 | 1.538 | 0.042 | 0.002 | FALSE | 1.512 |
| 10 | 10 | 10 | 0.2 | Regular | 0.7 | 0.5 | SS | 1.513 | 1.495 | 1.524 | 0.029 | 0.013 | TRUE | 1.512 |

| | | | | | | | | | | | | | | |
|---|---|---|---|---|---|---|---|---|---|---|---|---|---|---|
| 10 | 10 | 10 | 0.1 | Regular | 0.3 | 0.3 | SS | 1.514 | 1.526 | 1.555 | 0.028 | 0.034 | FALSE | 1.512 |
| 10 | 10 | 10 | 0.2 | Regular | 0.6 | 0.7 | SS | 1.507 | 1.471 | 1.497 | 0.026 | 0.070 | FALSE | 1.512 |
| 10 | 10 | 40 | 0 | Uneven | 0.7 | 0 | SS | 1.851 | 1.640 | 1.826 | 0.187 | 2.444 | FALSE | 2.014 |
| 10 | 10 | 40 | 0 | Regular | 0.7 | 0.9 | SS | 1.836 | 1.694 | 1.874 | 0.180 | 2.660 | FALSE | 2.014 |
| 10 | 10 | 40 | 0 | Regular | 0.7 | 0.8 | SS | 1.834 | 1.694 | 1.864 | 0.170 | 2.700 | FALSE | 2.014 |
| 10 | 10 | 40 | 0 | Regular | 0.7 | 0.7 | SS | 1.824 | 1.694 | 1.845 | 0.152 | 2.843 | FALSE | 2.014 |
| 10 | 10 | 40 | 0 | Regular | 0.7 | 0.5 | SS | 1.814 | 1.694 | 1.844 | 0.151 | 3.000 | FALSE | 2.014 |
| 5 | 5 | 40 | 0.1 | Uneven | 0.4 | 0.6 | CC | 5.170 | 3.267 | 5.433 | 2.165 | 0.002 | FALSE | 5.170 |
| 5 | 5 | 40 | 0.1 | Uneven | 0.3 | 0.8 | CC | 5.171 | 3.299 | 5.375 | 2.076 | 0.005 | FALSE | 5.170 |
| 5 | 5 | 10 | 0 | Uneven | 0.4 | 0.8 | CC | 5.169 | 3.394 | 5.285 | 1.891 | 0.022 | FALSE | 5.170 |
| 5 | 5 | 10 | 0.1 | Uneven | 0.4 | 0 | CC | 5.167 | 3.487 | 5.207 | 1.720 | 0.056 | FALSE | 5.170 |
| 5 | 5 | 10 | 0.1 | Uneven | 0.3 | 0 | CC | 5.160 | 3.515 | 5.205 | 1.690 | 0.159 | FALSE | 5.170 |

## 6. Discussion

### *6.1. Restoring Target-domain Coverage with Importance-weighted Conformal Prediction*

Split-conformal prediction (split-CP) achieves finite-sample marginal coverage by calibrating a single residual quantile threshold on a held-out calibration set under an exchangeability (IID) assumption. When deployment covariates differ from calibration e.g., switching BCs (SS→CC/CC→SS), holding out porosity patterns, AR bins, or geometry extremes the calibration residuals are drawn from a different covariate law than the target. In that case, the nominal 1−α quantile estimated on calibration is too low for the target domain, and intervals under-coverage. IW-CP corrects this by replacing the plain empirical quantile of calibration residuals with a weighted empirical quantile that reweights calibration points in proportion to how representative they are of the target covariate distribution $\hat{q}_{1-\alpha}^{IW} = inf\{q: \sum_{i\in C} \overline{w}_i\{r_i \le q\} \ge 1-\alpha\}$, $\overline{w}_i = w_i/\sum_{i\in C} w_j$ where $r_i$ are calibration residuals and $w_i = P_{test}(x_i)/P_{cal}(x_i)$ are density-ratio weights estimated via a balanced-prior logistic domain classifier. This simple substitution retargets the conformal threshold to the deployment distribution without retraining the predictor [70].

Across cross-BC transfers and regime holdouts, plain split-CP systematically under-covers relative to IID CV. For example, SS→CC drops Coverage@0.90 from ~0.90 to 0.84 (≈-6.2 pp), while CC→SS is milder at 0.86 (≈-4.2 pp). Regime holdouts show the same pattern i.e., pattern-out ≈0.85 (≈-5.2 pp), AR-bin-out ≈0.87 (≈-3.2 pp), and geometry-extremes ≈0.82 (≈-8.2 pp). Applying IW-CP lifts coverage to ≈0.89-0.90 in all cases (residual gaps≲1-2 percentage points), confirming that the failure mode is mis-targeted calibration rather than an inaccurate mean/quantile regressor. Point errors (MAE/RMSE) remain essentially unchanged, as expected calibration adjusts interval thresholds, not the predictor [74].

In general, coverage improvement is accompanied by a modest broadening of the intervals. Relative to IID CV width $W_{0.90}$≈0.58, IW-CP increases mean width by +0.02 to +0.06 in cross-BC and pattern/AR holdouts, and by +0.20 in geometry-extremes where data support is thinnest, an appropriate signal of higher epistemic uncertainty near design borders. To prevent unstable weights from driving spurious gains, weight clipping $[0.1, 10]$ was used, self-normalization and monitor effective sample size $ESS = (\sum \widetilde{w}_i)^2/\sum \widetilde{w}_i{}^2$, with a practical geometry extremes of $0.3n_{cal}$. When ESS approaches the geometry extremes, the observed width inflation is desirable rather than a defect.

IW-CP assumes a label-preserving covariate shift (same conditional $p(y|x)$, different $p(x)$. In the settings of the present study this is defensible (changing BC, pattern, AR, or geometry redistributes stiffness/mass without changing the physical definition of Ω. When future deployment departs more radically (e.g., new materials/loads not represented in the archive), IW-CP will still inflate widths to flag uncertainty but cannot guarantee nominal coverage without fresh calibration data. Practically, it is recommended to drift checks on incoming covariates, on-the-fly recalibration with IW-CP when drift is detected, and targeted data

augmentation near design borders to raise ESS and recover sharpness before committing to fabrication [66].

Classical approaches to covariate shift in regression include importance-weighted empirical risk minimization, re-sampling strategies, and domain adaptation methods that learn invariant representations (e.g., adversarial feature alignment or transductive fine tuning). These techniques modify or retrain the predictive model itself so that the conditional mapping better matches the target domain. In contrast, the present study keeps the gradient-boosted surrogate fixed and uses importance-weighted conformal prediction solely at the calibration layer to retarget residual quantiles to the deployment distribution. This choice is motivated by the goal of obtaining distribution-free, finite-sample valid prediction intervals under label-preserving shift, without repeatedly retraining the backbone model for each new deployment regime. In principle, importance-weighted training and representation level domain adaptation are complementary to IW-CP and could further reduce point error under shift, whereas IW-CP directly addresses the reliability (coverage) of the intervals.

### *6.2. Physics Alignment and Explainability*

On held-out predictions, permutation importance (40 repeats, 95% CIs) ranks BC as the dominant driver of Ω, followed by the physics-guided composites and the gradation indices. Porosity contributes to a smaller but non-negligible level consistent with the factor ranges in the design space. The PD curves confirm physics-consistent monotonic trends across the sampled ranges. Ω decreases with porosity and increases with taper and width. Ω also increases with $P_x$ and $P_z$ (and their composites) with diminishing returns at high ceramic fraction. Isotonic overlays provide a shape-constrained summary that suppresses finite-sample fluctuations without altering the learned directionality, as seen in Fig. 9. The tap×wid surface exhibits a cooperative increase in Ω as both levers increase, but with a soft ceiling near the upper envelope. This is precisely the saturation which designers encounter when co-tuning section geometry under constraints as seen in Fig. 10. A lightweight sign-check on smoothed PD derivatives demonstrate 0% violations for porosity and taper and only ≈1.7% for width, localized near design edges where support thins. Isotonic overlays "repair" these small artifacts while preserving the trends (Fig. 11). Across global importance, PD effect summaries and monotonic assessment, the surrogate's mechanisms align with expected vibration physics. BC and gradation dominate, porosity lowers Ω, and geometry (taper/width) rises with diminishing returns. These diagnostics justify the model validation prescriptions in the risk-aware design stage, where calibrated widths penalize overly aggressive geometry at the envelope [64].

### *6.3. Vibration Behaviour of FGPTB and Empirical Trends*

The empirical trends align with graded-beam mechanics. BC is the single largest driver in which CC configurations yield higher Ω than SS across the lattice (consistent with greater kinematic restraint), which also explains the SS to CC transfer being harsher than CC to SS. Porosity monotonically reduces Ω, at fixed $\alpha$, uneven patterns reduces Ω more than even patterns, matching the pattern-out and hold-out ordering. Gradation increases Ω through both directions, $P_z$ (thickness-wise, biasing stiff material toward the faces) boosts bending rigidity strongly at moderate values and saturates at high $P_z$. $P_x$ (along-span) provides small increase with similar saturation. Geometry levers are monotone where they increase with taper (tap) and width (wid) over their feasible ranges, with diminishing returns near the upper envelope [54]. The tap×wid surface shows cooperative gains but a soft ceiling, which single-factor plots understate. Slenderness acts as expected, larger AR lowers Ω using 1/AR as a feature captures the positive direction of change. These are consistent with the PD diagnostics and the interaction surface summarized in Figs. 9 and 10.

Relative to the IID baseline, cross-BC differences are the most pronounced (coverage gaps and width responses), while geometry extremes show the largest widening of calibrated intervals. At the same time, point errors remain stable across regimes, reinforcing that reliability shifts stem from calibration rather than degradation of the mean predictor (Figs. 4 and 5).

Under the feasibility conditions, low Ω targets are met with modest tap/wid and low $\alpha$ narrow

calibrated widths. Mid Ω targets often require either relaxing $\alpha$/tap/wid or switching BC/AR. High Ω targets trigger interval inflation on the Pareto plane, correctly warning of limited capacity unless constraints or data coverage are expanded.

### *6.4. Practical Implications*

The empirical trends and calibrated intervals provide direct guidance for vibration-oriented design of FGPTB. The strong dominance of boundary condition and gradation implies that, for a given footprint, designers should first tune support conditions and ceramic richness (via $P_x$,$P_z$, or $GI_{sum}/GI_{prod}$) to place Ω in the desired band, using porosity and taper/width as secondary levers for fine adjustment. The monotone decrease of Ω with porosity and the modest increase with taper indicate that aggressive porosity or taper combinations can be used to reduce mass or increase stiffness only up to the point where calibrated intervals remain acceptably narrow. The inverse design fronts further show how low and moderate target frequencies can be achieved with tight, well-calibrated intervals, whereas attempting very high targets under strict manufacturability constraints leads to interval inflation and signals limited design capacity. In practice, the surrogate and its calibrated intervals can therefore be used as a screening tool. Designs that meet both frequency and interval width criteria are carried forward to higher accuracy analysis or prototyping, while designs that require large extrapolation or exhibit wide intervals are flagged as risky for further investigation rather than immediate manufacture.

### *6.5. Comparison with Prior Work*

Classical vibration analyses of FGPBs and FGPs, including those by [17,18,21,23] have established accurate deterministic predictions for Ω under refined kinematics, viscoelasticity and stochastic material variations, but they do not provide data-driven surrogates or calibrated uncertainty under deployment shifts. More recent ML and studies based on boosting FGM/FGP vibration demonstrate that neural networks, GPR and tree ensembles can approximate eigen frequencies with high in-distribution accuracy, and approaches based on PINN [38,-40] embed governing equations into neural solvers. However, these works typically focus on point prediction and assume nominal deployment regimes. The present study differs in that it uses a FGPTB model based on HSDT as a generator of labelled data across BCs, porosity patterns, and geometric shifts. It builds a gradient-boosted surrogate equipped with split and importance-weighted conformal calibration to deliver finite-sample valid prediction intervals under label-preserving covariate shift. It integrates these calibrated intervals into a risk-aware inverse design workflow on a practicable design lattice. Thus, the proposed methodology complements existing deterministic and FGM vibration studies on ML by making reliability under shift and decision layer trade-offs explicit.

## 7. Limitations of the Study

While the proposed methodology demonstrates strong predictive accuracy, calibrated uncertainty, and physics-aligned design guidance, several factors bound the generality of the present findings:

- The HSDT formulation is linear elastic, undamped, and restricted to free vibration. Load-dependent stiffness, temperature dependence, viscoelasticity, foundation effects, geometric imperfections, and material nonlinearity (e.g., elasto-plasticity) are not modelled, so the surrogate is currently valid only for idealized linear free vibration scenarios of FGPTB.
- The dataset is generated on a bounded Cartesian lattice in gradient indices, porosity level/pattern, aspect ratio, and taper/width ratios. Outside these prescribed ranges, especially near geometric or porosity extremes, epistemic uncertainty grows and manifests as wider calibrated intervals. Extrapolation beyond the sampled design space should therefore be treated with caution.
- Conformal prediction provides marginal coverage guarantees, not strict conditional coverage for every slice of the input space. For small or highly unbalanced sub-regimes, empirical coverage may deviate from nominal despite overall reliability.
- Importance-weighted conformal prediction assumes label-preserving covariate shift and sufficient overlap between calibration and

target covariate distributions. Under very strong deployment drift or poor overlap, density ratio estimation becomes fragile, and the coverage guarantees may deteriorate.

- The inverse design is performed over a discrete feasible lattice and knee point selection on the error width plane. This is practical and reproducible, but it is not equivalent to solving a fully continuous, constrained multi-objective optimization problem. Some potentially optimal continuous designs may lie between lattice points.
- All data is generated from an HSDT-based numerical model. No experimental FGPTB vibration measurements are used for external validation. The surrogate therefore inherits any modelling bias present in the underlying theory and numerical implementation.

## 8. Conclusions

This study developed a shift-robust, ML surrogate and design methodology for the free-vibration response of functionally graded porous tapered beams. The study unifies importance-weighted conformal calibration to maintain nominal reliability under covariate shift, stress-tested generalization across boundary conditions and regime holdouts. Physics-aware explainability via permutation importance, 1D/2D partial dependence with isotonic overlays, a monotonic assessment and a risk-aware inverse-design workflow that selects designs on the Pareto front of absolute error versus calibrated interval width under manufacturability constraints. Together, these components convert calibrated uncertainty into actionable design choices without recourse of other solution methods. The key findings of this study are as follows:

- Across 5-fold cross-validation, errors are uniformly small with MAE=0.56 and RMSE=0.91 and $R^2$=0.9996 with low cross-fold variance, evidencing a stable sample-efficient surrogate. This affirms high predictive accuracy on non-dimensional natural frequency.
- Reliability recovered under shift via IW-conformal demonstrated that split-conformal produces under coverage cross- and regime-holdouts. Importance-weighted residual quantiles restore coverage toward the nominal 0.90 with only marginal changes in mean interval width.
- Cross-boundary condition transfer remains accurate and reliable that the SS to CC and CC to SS transfers incur modest accuracy penalties relative to independent and identically distributed cross-validation, while IW-conformal closes most of the coverage gap demonstrating practical robustness to support changes.
- Monotonic assessment is nearly satisfied that the sign-violation rates are ~0% for porosity and taper and ≲2% for width and isotonic overlays "repair" residual fluctuations while preserving the trends.
- On the constrained lattice (porosity≤ 0.20, tap ≤ 0.70), Pareto error width fronts yield knee designs that balance closeness to target and interval width. Low natural frequency targets are reachable with tight CI, mid natural frequency targets recommend relaxing porosity/aspect ratio/taper and high natural frequency targets trigger large widths.
- Mechanistic coherence for FGPTB vibrations infers that uneven porosity patterns decrease natural frequency more than even patterns, increasing ceramic-lean grading indices rise stiffness/natural frequency with saturation and slenderness reduces natural frequency.

The study delivers a compact, explainable, and deployable ML surrogate for FGPTB vibration, pairing calibrated reliability with inverse-design utility across in-distribution and shifted regimes. The vibration model can be enriched by incorporating damping, thermal loading, viscoelastic effects, foundation interactions and realistic pore morphologies so that the surrogate remains valid under manufacturing variability and service conditions. Future work will focus on addressing these limitations in several directions:

1) Enriching the vibration model to include damping, thermal loading, viscoelastic and foundation effects, and more realistic pore morphologies so that the surrogate remains valid under manufacturing variability and service conditions.
2) Broadening the parametric space to cover wider ranges of gradation indices, porosity patterns, taper/width ratios and additional

boundary conditions, and extending the surrogate to higher modes and coupled responses such as buckling or stress fields.

3) Pairing importance-weighted conformal prediction with drift detection and on-the-fly recalibration to manage stronger deployment shifts and exploring alternative calibrated learners such as monotone constrained boosting or Bayesian ensembles.
4) Moving from a discrete design lattice to continuous, constrained multi-objective optimization that jointly targets natural frequency, mass and manufacturability, and
5) Performing high-accuracy 3D simulations and, ultimately, experimental vibration tests on manufactured FGPTB specimens to externally validate and refine the surrogate.
6) Combined strategies in which the surrogate is first trained using importance-weighted empirical risk minimization under covariate shift and subsequently recalibrated with IW-CP, with the aim of jointly improving pointwise accuracy and interval coverage in the target domain.
7) Extend the present lattice-based inverse design to a fully continuous, constrained multi-objective optimization method in which the design vector is treated as continuous, and evolutionary or gradient-based solvers are coupled to the calibrated surrogate to search for designs that minimize both frequency error and interval width

## Nomenclature

| | |
|---|---|
| AR | Aspect ratio |
| BC | Boundary Condition |
| CBT | Classical beam theory |
| CC | Clamped-Clamped |
| CI | Confidence Interval |
| CP | Conformal Prediction |
| CQR | Conformalized Quantile Regression |
| CV | Cross-validation |
| ECE | Expected Calibration Error |
| ESS | Effective sample size |
| FGB | Functionally graded beam |
| FGM | Functionally graded materials |
| FGPB | Functionally graded porous beam |
| FGPTB | Functionally graded porous taper beam |
| FSDT | First-order shear deformation theory |
| GBDT | Gradient-Boosted Decision Trees |
| GPR | Gaussian-process regression |
| HSDT | Higher-order shear deformation theory |
| IID | Independent and Identically Distributed |
| IW-CP | Importance-weighted Conformal Prediction |
| MAE | Mean Absolute Error |
| ML | Machine Learning |
| PD | Partial dependence |
| RMSE | Root Mean Squared Error |
| $R^2$ | Coefficient of Determination |
| RSM | Response-surface methodology |
| SHAP | SHapley Additive exPlanations |
| SS | Simply Supported |
| $a$ | The single raw value for a feature |
| $B$, $B_s$ | The strain-displacement operators |
| $E(x,z)$ | Effective Young's modulus |
| $f(z)$ | The shear shape function |
| $\hat{f}$ | The trained predictor |
| $g(z;h)$ | The shear shape derivative |
| $GI_{sum}$ | Gradation index sum |
| $GI_{prod}$ | Gradation index product |
| $h_t$ | The shallow classification |
| $J_1(x)$ | The accuracy objective |
| $J_2(x)$ | The risk (uncertainty) objective |
| $L$ | The length of the beam |
| $n$ | The number of test samples |
| $P_x, P_z$ | Bi-directional gradient indices |
| $s_i$ | The nonconformity score |
| $s(x)$ | The logistic domain classifier |
| $t_1, t_2$ | The time intervals |
| $T$ | The kinetic energy |
| $u_0(x)$ | The axial displacement at the neutral axis of the beam |
| $u(x,z)$ | The axial displacement |
| $U$ | The strain energy |
| $V_m(x,z)$ | The volume fraction of the metal |
| $V_c(x,z)$ | The volume fraction of the ceramic |
| $w(x,z)$ | The transverse displacement |
| $w(x)$ | The importance weight |
| $\alpha$ | The porosity index |
| $\beta$ | The quantile GBDT head |
| $\mu_a$ | The mean of that feature |
| $\hat{\mu}(x)$ | The mean regressor |
| $\varepsilon_x$ | The non- zero axial strain |
| $\gamma_{xz}$ | The shear strain in the *x*-*z* plane |
| $\sigma_x$ | The Unilateral stress |
| $\tau_{xz}$ | The shear stress in the *x*-*z* plane |
| $\sigma_a$ | The standard deviation of that feature |
| $\eta$ | The learning rate |

| | |
|---|---|
| $\emptyset(x)$ | The rotation of the cross-section due to bending |
| $\rho(x,z)$ | Effective mass density |
| $\nu(x,z)$ | Effective Poisson's ratio |
| $\Omega$ | The non-dimensional natural frequency |
| $\widehat{\Omega}$ | The model-predicted non-dimensional natural frequency |
| $\overline{\Omega}$ | The mean of the true non-dimensional natural frequencies |
| $\widehat{PD}_{iso}$ | Isotonic overlay of PD |
| $\Delta_{iso}$ | Isotonic deviation |

## Funding Statement

This research did not receive any specific grant from funding agencies in the public, commercial, or not-for-profit sectors.

## Conflicts of Interest

The author declares that there is no conflict of interest regarding the publication of this article.

## Data availability

The dataset used in this study (design lattice and corresponding non-dimensional natural frequencies) is provided as Supplementary Material to facilitate independent analysis and reuse.

## References

[1] Le, Q.C. and Nguyen, B.D., 2025. Two-dimensional Elasticity Solutions For Analyzing Free Vibration Of Functionally Graded Porous Beams. *Mechanics of Advanced Composite Structures*, *12*(1), pp.235-248.

[2] Nazemnezhad, R., 2024. A semi-analytical nonlinear approach for size-dependent analysis of longitudinal vibration in terms of axially functionally graded nanorods. *Mechanics of Advanced Composite Structures*, *11*(2), pp.453-466.

[3] Nazemnezhad, R., Razavian Shad, E. and Jandaghian, A.A., 2024. Nonlinear torsional vibration of size-dependent functionally graded rods. *Mechanics of Advanced Composite Structures*, *11*(1), pp.41-58.

[4] Kumar, R., Sharma, H.K., Gupta, S., Malguri, A., Rajak, B., Srivastava, Y., Khan, S. and Pandey, A., 2024. Initial buckling behavior of elastically supported rectangular FGM plate based on higher order shear deformation theory via spline RBF method. *Mechanics of Advanced Composite Structures*, *11*(1), pp.59-72.

[5] Kannaiyan, G.N, Balasubramaniam, V., Pappula, B., and Makgato, S., 2024. Novel Kuhn-Tucker conditions for vibration analysis in a functionally graded porous beam using the R-program. *Results in Engineering*, 22, 102064.

[6] Turan, M., 2024. Mixed series solution for vibration and stability of porous bi-directional functionally graded beams. *Archive of Applied Mechanics*, 94(6), pp. 1785-1806.

[7] Bagheri, Z., Fiouz, A., and Seraji, M., 2024. Effect of porosity on free vibration and buckling of functionally graded porous beams with non-uniform cross-section. *Journal of Central South University*, 31(3), pp. 841-857.

[8] Wu, S., Li, Y., Bao, Y., Zhu, J., and Wu, H., 2024. Examination of beam theories for buckling and free vibration of functionally graded porous beams. *Materials*, 17(13), 3080.

[9] Burlayenko, V.N., Altenbach, H., and Dimitrova, S.D., 2024. Modal characteristics of functionally graded porous Timoshenko beams with variable cross-sections. *Composite Structures*, 342, 118273.

[10] Mantari, J.L., Yarasca, J., Canales, F.G. and Arciniega, R.A., 2019. New methodology for the construction of best theory diagrams using neural networks and multi-objective genetic algorithm. *Composites Part B: Engineering*, *176*, p.107126.

[11] Cuba, LM, Arciniega, RA & Mantari, JL 2019, 'Generalized 2-unknown's HSDT to study isotropic and orthotropic composite plates', *Journal of Applied and Computational Mechanics*, vol. 5, no. 1, pp. 141-149.

[12] Vu, T.V., Nguyen-Van, H., Nguyen, C.H., Nguyen, T.P. and Curiel-Sosa, J.L., 2023. Meshfree analysis of functionally graded plates with a novel four-unknown arctangent exponential shear deformation theory. *Mechanics Based Design of Structures and Machines*, *51*(2), pp.1082-1114.

[13] Mantari, JL & Guedes Soares, C 2015, 'Five-unknowns generalized hybrid-type quasi-3D HSDT for advanced composite plates', *Applied Mathematical Modelling*, vol. 39, no. 18, pp. 5598-5615.

[14] Mantari, JL & Granados, EV 2015, 'Thermoelastic analysis of advanced sandwich plates based on a new quasi-3D hybrid type HSDT with 5 unknowns', *Composites Part B: Engineering*, vol. 69, pp. 317-334.

[15] Mantari, JL & Granados, EV 2015, 'Thermoelastic behavior of advanced composite sandwich plates by using a new 6 unknown quasi-3D hybrid type HSDT', *Composite Structures*, vol. 126, pp. 132-144.
[16] Canales, FG & Mantari, JL 2017, 'Elasto-plastic vibrational analysis of tapered bars under uniform axial loading considering shear deformation and rotary inertia', *International Journal of Non-Linear Mechanics*, vol. 95, pp. 103-116.
[17] Vo, T.P., Thai, H.T., Nguyen, T.K. and Inam, F., 2014. Static and vibration analysis of functionally graded beams using refined shear deformation theory. *Meccanica*, *49*(1), pp.155-168.
[18] Vo, T.P., Thai, H.T., Nguyen, T.K., Maheri, A. and Lee, J., 2014. Finite element model for vibration and buckling of functionally graded sandwich beams based on a refined shear deformation theory. *Engineering structures*, *64*, pp.12-22.
[19] Mesbah A, Belabed Z, Amara K, Tounsi A, Bousahla AA, and Bourada F., 2023. Formulation and evaluation a finite element model for free vibration and buckling behaviours of functionally graded porous (FGP) beams. *Structural Engineering and Mechanics, 86(3)*, pp. 291-309.
[20] Wang, X. and Li, S., 2016. Free vibration analysis of functionally graded material beams based on Levinson beam theory. *Applied Mathematics and Mechanics*, *37*(7), pp.861-878.
[21] Chen, D., Yang, J. and Kitipornchai, S., 2016. Free and forced vibrations of shear deformable functionally graded porous beams. *International journal of mechanical sciences*, *108*, pp.14-22.
[22] Chen, D., Gao, K., Yang, J. and Zhang, L., 2023. Functionally graded porous structures: analyses, performances, and applications–a review. *Thin-Walled Structures*, *191*, p.111046.
[23] Wu, H., Yang, J. and Kitipornchai, S., 2020. Mechanical analysis of functionally graded porous structures: A review. *International Journal of Structural Stability and Dynamics*, *20*(13), p.2041015.
[24] Eiadtrong, S., Wattanasakulpong, N. and Vo, T.P., 2023. Thermal vibration of functionally graded porous beams with classical and non-classical boundary conditions using a modified Fourier method. *Acta Mechanica*, *234*(2), pp.729-750.
[25] Nguyen, N.D., Nguyen, T.N., Nguyen, T.K. and Vo, T.P., 2022. A new two-variable shear deformation theory for bending, free vibration and buckling analysis of functionally graded porous beams. *Composite Structures*, *282*, p.115095.
[26] Jia, S., Yang, G., Pu, Y., Ma, P. and Li, K., 2025. Free Vibration Characteristics of Functionally Graded Material (FGM) Beams on Three-Parameter Viscoelastic Foundation. *Journal of Composites Science*, *9*(5), p.215.
[27] Singh, A., Naskar, S., Kumari, P. and Mukhopadhyay, T., 2023. Viscoelastic free vibration analysis of in-plane functionally graded orthotropic plates integrated with piezoelectric sensors: Time-dependent 3D analytical solutions. *Mechanical Systems and Signal Processing*, *184*, p.109636.
[28] Cui, Y., Zeng, T., Yang, Y., Wang, X., Xu, G. and Cheng, S., 2025. A Time-Domain Solution Method for the Vibration Performance of Viscoelastic Functionally Graded Porous Beams. *Vibration*, *8*(2), p.28.
[29] Kadioglu, H.G. and Yayli, M.O., 2025. Axial vibration of a viscoelastic FG nanobeam with arbitrary boundary conditions. *Journal of Vibration Engineering & Technologies*, *13*(1), p.96.
[30] Alnujaie, A., Akbas, S.D., Eltaher, M.A. and Assie, A., 2021. Forced vibration of a functionally graded porous beam resting on viscoelastic foundation. *Geomechanics & engineering*, *24*(1), pp.91-103.
[31] Shegokar, N.L. and Lal, A., 2013. Stochastic Nonlinear Free Vibration Analysis of Functionally Graded Beam Subjected to Thermal Loading with Random Material Properties. *Advanced Materials Research*, *747*, pp.551-554.
[32] Chandel, V.S. and Talha, M., 2022. Stochastic thermo-elastic vibration characteristics of functionally graded porous nano-beams using first-order perturbation-based nonlocal finite element model. *Proceedings of the Institution of Mechanical Engineers, Part C: Journal of Mechanical Engineering Science*, *236*(15), pp.8563-8581.
[33] Wu, C.P., Yeh, S.T. and Liu, J.H., 2023. A Nonlinear Free Vibration Analysis of Functionally Graded Beams Using a Mixed Finite Element Method and a Comparative Artificial Neural Network. *Journal of Composites Science*, *7*(6), p.229.
[34] Tariq, A., Uzun, B., Deliktaş, B. and Yaylı, M.Ö., 2025. Application of machine learning methodology for investigating the vibration behavior of functionally graded porous nanobeams. *The Journal of Strain Analysis for Engineering Design*, *60*(2), pp.131-151.
[35] Tariq, A., Uzun, B., Akpinar, M., Yayli, M.O. and Deliktas, B., 2025. Size dependent dynamics of a bi-directional functionally

graded nanobeam via machine learning methods. *Advances in nano research*, *18*(1), pp.33-52.

[36] Tariq, A., Uzun, B., Deliktaş, B. and Yaylı, M.Ö., 2024. Vibration analysis of embedded porous nanobeams under thermal effects using boosting machine learning algorithms and semi-analytical approach. *Mechanics of advanced materials and structures*, *31*(29), pp.12320-12343.

[37] Eshaghi, M.S., Bamdad, M., Anitescu, C., Wang, Y., Zhuang, X. and Rabczuk, T., 2025. Applications of scientific machine learning for the analysis of functionally graded porous beams. *Neurocomputing*, *619*, p.129119.

[38] Söyleyici, C. and Ünver, H.Ö., 2025. A Physics-Informed Deep Neural Network based beam vibration framework for simulation and parameter identification. *Engineering Applications of Artificial Intelligence*, *141*, p.109804.

[39] Mirsadeghi Esfahani, S.S., Fallah, A. and Mohammadi Aghdam, M., 2025. Physics-Informed Neural Network for Nonlinear Bending Analysis of Nano-Beams: A Systematic Hyperparameter Optimization. *Mathematical and Computational Applications*, *30*(4), p.72.

[40] Zhang, X., Zhu, H. and Xu, W., 2025. Dynamic Response Prediction of a Cantilever Beam Under Different Boundary Constraints and Excitation Conditions Based on an Improved Physics-Informed Neural Network. *The Structural Design of Tall and Special Buildings*, *34*(2), p.e70002.

[41] Minh, H.L., Sang-To, T., Le-Van, B. and Cuong-Le, T., 2025. A novelty solution for orthotropic composite plate based on physics informed neural network. *Frontiers of Structural and Civil Engineering*, pp.1-24.

[42] Martinez, Y., Rojas, L., Peña, A., Valenzuela, M. and Garcia, J., 2025. Physics-Informed Neural Networks for the Structural Analysis and Monitoring of Railway Bridges: A Systematic Review. *Mathematics*, *13*(10), p.1571.

[43] Bridjesh, P., Geetha, N.K., and Yelamasetti, B., 2024. Numerical investigation on buckling of two-directional porous functionally graded beam using higher order shear deformation theory. *International Journal on Interactive Design and Manufacturing*, 18(5), pp. 2805-2818.

[44] Müsevitoğlu, A., Özütok, A., and Reddy, J.N., 2025. Static analysis of functionally graded and laminated composite beams using various higher-order shear deformation theories: A study with mixed finite element models. *European Journal of Mechanics-A/Solids*, 111, 105596.

[45] Bridjesh, P., Geetha, N.K., and Reddy, G.C.M., 2023. On Numerical Investigation of Buckling in Two-Directional Porous Functionally Graded Beam Using Higher Order Shear Deformation Theory. *Mechanics of advanced composite structures,* 10(2), pp. 393-406.

[46] Echouai, B., Adri, A., El Khouddar, Y., Outassafte, O., El Hantati, I., kouchi Echouai, E., Hassa, M., and Benamar, R., 2025. Analysis of transverse vibrations of functionally graded beams with magnetostrictive Terfenol-D layers resting on an elastic foundation. *Scientific African*, e02651.

[47] Özmen, U., and Özhan, B.B., 2025. Mechanics of functionally graded beams: analytical, computational, and experimental analyses. *International Journal of Mechanics and Materials in Design*, 21(3), pp. 577-590.

[48] Garg, A., Fantuzzi, N., Avcar, M., and Li, L., 2025. High-fidelity surrogate-driven h-refined IGA for free vibration analysis of laminated composite annular plates with radial and curved cracks. *Archives of Civil and Mechanical Engineering*, 25(4), 225.

[49] Rizkallah, L.W., 2025. Enhancing the performance of gradient boosting trees on regression problems. *Journal of big data*, 12(1), 35.

[50] Uyar, S.G., Ozbay, B.K., and Dal, B., 2025. Interpretable building energy performance prediction using XGBoost Quantile Regression. *Energy and Buildings*, 340, 115815.

[51] Sluijterman, L., Kreuwel, F., Cator, E., and Heskes, T., 2025. Composite quantile regression with XGBoost using the novel arctan pinball loss. *International Journal of Machine Learning and Cybernetics*, pp. 1-15.

[52] Qin, J., Piao, J., Ning, J., and Shen, Y., 2025. Conformal predictive intervals in survival analysis: a resampling approach. *Biometrics*, 81(2), ujaf063.

[53] Qin, J., Liu, Y., Li, M., and Huang, C.Y., 2025. Distribution-free prediction intervals under covariate shift, with an application to causal inference. *Journal of the American Statistical Association*, 120(549), pp. 559-571.

[54] Jia, S., Yang, G., Pu, Y., Ma, P., and Li, K., 2025. Free Vibration Characteristics of Functionally Graded Material (FGM) Beams on Three-Parameter Viscoelastic Foundation. *Journal of Composites Science*, 9(5), 215.

[55] Ali, M.I., Azam, M.S., Ranjan, V., and Banerjee, J.R., 2025. Free vibration of moderately thick FGM plates using the dynamic stiffness

method and the Wittrick-Williams algorithm. *Computers & Structures*, 317, 107885.

[56] Taima, M.S., El-Sayed, T.A., and Friswell, M.I., 2025. Dynamic stability analysis of tapered rotating beams with 2D functionally graded materials: a comparative study of Floquet theory approaches. *Thin-Walled Structures*, 213, 113257.

[57] Hadrich, A., Zghal, S., Koubaa, S., and Bouaziz, Z., 2025. Free vibration of functionally graded porous perforated solid structures with complex shaped holes. *International Journal of Solids and Structures*, 113449.

[58] Huang, P.H., 2025. Residual permutation tests for feature importance in machine learning. *British Journal of Mathematical and Statistical Psychology*.

[59] Rosenblad, A.K., 2025. A note on two novel easy-to-interpret feature effect measures for partial dependence plots in a classification setting. *Journal of Applied Statistics*.

[60] Choi, D., 2025. Unbiased Isotonic Regression Tree for Discovering Hidden Heterogeneity in Monotonicity Constraints. *Applied Sciences*, 15(2), 818.

[61] Meijerink, L.M., Schuit, E., Moons, K.G., and Leeuwenberg, A.M., 2025. Plug-and-play use of tree-based methods: Consequences for clinical prediction modelling. *Journal of Clinical Epidemiology*, 111834.

[62] Liao, V., and Jayaraman, A., 2025. Inverse Design of Block Polymer Materials with Desired Nanoscale Structure and Macroscale Properties. *JACS Au*, 5(6), pp. 2810–2824.

[63] Tamuly, P., and Nava, V., 2025. Machine learning based conformal predictors for uncertainty-aware compressive strength estimation of concrete. *Construction and Building Materials*, 487, 141844.

[64] De Temmerman, A., and Verbeke, M., 2025. Improved multi-objective decision-making in manufacturing processes through uncertainty quantification and robust pareto front modelling. *Scientific Reports*, 15(1), 14411.

[65] Shmuel, A., Glickman, O., and Lazebnik, T., 2025. A comprehensive benchmark of machine and deep learning models on structured data for regression and classification. *Neurocomputing*, 131337.

[66] Solís-Martín, D., Galán-Páez, J., and Borrego-Díaz, J., 2025. A Model for Learning-Curve Estimation in Efficient Neural Architecture Search and Its Application in Predictive Health Maintenance. *Mathematics*, 13(4), 555.

[67] Karimi-Asrami, A., and Jafari-Talookolaei, R.A., 2025. Free and forced vibration analysis of functionally graded porous frames. *Engineering Computations*, 42(4), pp. 1417-1446.

[68] Sharma, P., Sharma, A., and Parashar, S.K., 2025. Shear actuated vibration analysis of Bi-directional FGP non-uniform beam using generalized differential quadrature method. *Mechanics Based Design of Structures and Machines*, 53(7), pp. 5210-5233.

[69] Msaddi, S., and Kumbasar, T., 2025. Expanding conformal prediction to system identification. *Pattern Recognition*, 111758.

[70] El-Shahrany, H.D., 2025. Porosity-Dependent Frequency Analysis of Bidirectional Porous Functionally Graded Plates via Nonlocal Elasticity Theory. *Mathematics*, 13(16), 2688.

[71] Omar, O.K., Alshawabkeh, M., and Alkhatib, H., 2025. Closed form solutions of bending Bi-directional functionally graded tapered beams using Euler and Timoshenko theories. *Results in Engineering*, 25, 104204.

[72] Yin, M., Shi, C., Wang, Y., and Blei, D.M., 2024. Conformal sensitivity analysis for individual treatment effects. *Journal of the American Statistical Association*, 119(545), pp. 122-135.

[73] Li, Y., Goodrich, J.M., Peterson, K.E., Song, P.X., and Luo, L., 2025. Uncertainty quantification in epigenetic clocks via conformalized quantile regression. *Genetic Epidemiology*, 49(4), e70008.

[74] Shi, Y., Wei, P., Feng, K., Feng, D.C, and Beer, M., 2025. A survey on machine learning approaches for uncertainty quantification of engineering systems. *Machine Learning for Computational Science and Engineering*, 1(1), 11.